REFERENCES

Berlin, G. L., M. A. Tarabzouni, A. H. Al-Naser, K. M. Sheikho, and R. W. Larson, 1986, SIR-B subsurface imaging of a sand-buried landscape—Al Labbah Plateau, Saudi Arabia: IEEE Transactions on Geoscience and Remote Sensing, v. GE-24, p. 595–602.

Blom, R. G., R. E. Crippen, and C. Elachi, 1984, Detection of subsurface features in Seasat radar images of Means Valley, Mojave Desert, California: Geology, v. 12, p. 346–349.

Cimino, J. B. and C. Elachi, eds., 1982, Shuttle imaging radar–A (SIR-A) experiment: Jet Propulsion Laboratory Publication 82-77, Pasadena, CA.

Cimino, J. B., B. Holt, and A. H. Richardson, 1988, The Shuttle imaging radar–B (SIR-B) experiment report: Jet Propulsion Laboratory Report 88-10, Pasadena, CA.

European Space Agency, 1993, ERS user handbook: European Space Agency SP-1148, Revision 1, Noordwick, Netherlands.

Evans, D. L. and others, 1994, Earth from sky: Scientific American, v. 271, p. 70–75.

Ford, J. P., ed., 1988, Advances in Shuttle imaging radar–B research: Taylor and Francis Group, Bristol, PA.

Ford, J. P., R. G. Blom, M. L. Bryan, M. I. Daily, T. H. Dixon, C. Elachi, and E. C. Xenos, 1980, Seasat views North America, the Caribbean, and western Europe with imaging radar: Jet Propulsion Laboratory Publication 80-67, Pasadena, CA.

Ford, J. P., J. B. Cimino, and C. Elachi, 1983, Space Shuttle Columbia views the world with imaging radar—the SIR-A experiment: Jet Propulsion Laboratory Publication 82-95, Pasadena, CA.

Ford, J. P., J. B. Cimino, B. Holt, and M. R. Ruzek, 1986, Shuttle imaging radar views the earth from Challenger—the SIR-B experiment: Jet Propulsion Laboratory Publication 86-10, Pasadena, CA.

Ford, J. P. and F. F. Sabins, 1986, Satellite radars for geologic mapping in tropical regions: Environmental Research Institute of Michigan Fifth Thematic Conference, Remote Sensing for Geology, Proceedings, Ann Arbor, MI.

Ford, J. P. and others, 1989, Spaceborne radar observations—A guide for Magellan radar image analysis: Jet Propulsion Laboratory Publication 89-41, Pasadena, CA.

Ford, J. P. and others, 1993, Guide to Magellan image interpretation: Jet Propulsion Laboratory Publication 93-24, Pasadena, CA.

Head, J. W. and others, 1992, Venus volcanism—classification of volcanic features and structures, associations, and global distribution from Magellan data: Journal of Geophysical Research, v. 97, p. 13,153–13,197.

Lalonde, L., G. Posehn, and F. F. Sabins, 1993, Comparison and evaluation of ERS-1 and airborne radar images: Environmental Research Institute of Michigan, Ninth Thematic Conference on Geologic Remote Sensing, Proceedings, p. 21–33, Ann Arbor, MI.

McCauley, J. F. and others, 1982, Subsurface valleys and geoarcheology of the eastern Sahara revealed by Shuttle radar: Science, v. 318, p. 1004–1020.

Nazarenko, D., G. Staples, and C. Aspden, 1996, Radarsat—first images: Photogrammetric Engineering and Remote Sensing, v. 62, p. 143–146.

Radarsat International, 1995, Radarsat illuminated—your guide to products and services: Radarsat International, Richmond, B.C., Canada.

Sabins, F. F., 1983, Geologic interpretation of Space Shuttle radar images of Indonesia: American Association of Petroleum Geologists Bulletin, v. 67, p. 2076–2099.

Sabins, F. F., R. Blom, and C. Elachi, 1980, Seasat radar images of San Andreas fault, California: American Association of Petroleum Geologists Bulletin, v. 64, p. 619–628.

Schaber, G. G., J. F. McCauley, C. S. Breed, and G. R. Olhoeft, 1986, Shuttle imaging radar—Physical controls on signal penetration and subsurface scattering in the eastern Sahara: IEEE Transactions on Geoscience and Remote Sensing, v. GE-24, p. 603–623.

Schaber, G. G. and others, 1992, Geology and distribution of impact craters on Venus—what are they telling us?: Journal of Geophysical Research, v. 97, p. 13,257–13,301.

Solomon, S. C. and others, 1992, Venus tectonics—an overview of Magellan observations: Journal of Geophysical Research, v. 97, p. 13,199–13,255.

Strom, R. G., G. G. Schaber, and D. D. Dawson, 1994, The global resurfacing of Venus: Journal of Geophysical Research, v. 99, p. 10,899–10,926.

ADDITIONAL READING

Elachi, C., 1987, Spaceborne radar remote sensing—applications and techniques: IEEE Press, New York, NY.

Evans, D. and A. Freeman, 1995, Future directions for synthetic aperture radar: Proceedings, Land Satellite Information in the Next Decade, American Society for Photogrammetry and Remote Sensing, Falls Church, VA.

Ivanov, M. A. and J. W. Head, 1996, Tessera terrain on Venus—a survey of the global distribution, characteristics, and relation to surrounding units from Magellan data: Journal of Geophysical Research, v. 1012, p. 14,861–14,908.

Nishidai, T., 1993, Early results from Fuyo-1, Japan's Earth Resources Satellite (JERS-1): International Journal of Remote Sensing, v. 14, p. 1825–1833.

Raney, R. K. and others, 1991, Radarsat, IEEE Proceedings, v. 79, p. 839–849.

Sabins, F. F. and J. P. Ford, 1985, Space Shuttle radar images of Indonesia: Indonesian Petroleum Association, Proceedings, 14th annual convention, p. 470–476, Jakarta, Indonesia.

Saunders, R. S. and G. H. Pettengill, 1991, Magellan—mission summary: Science, v. 252, p. 247–249.

Singhroy, V. and others, 1993, Radarsat and radar geology in Canada: Canadian Journal of Remote Sensing, v. 19, p. 338–351.

depression angle, polarization, and ground resolution cell. Explain your choices.

CHAPTER

8

DIGITAL IMAGE PROCESSING

Most remote sensing images are recorded in digital form and then processed by computers to produce images for interpreters to study. Less than a decade ago digital image processing was essentially confined to dedicated facilities with expensive mainframe computers operated by staffs of specialists. Today images can be processed with inexpensive desktop computers and software by users with average computer skills.

Digital processing did not originate with remote sensing and is not restricted to these data. Many image-processing techniques were developed in the medical field to process X-ray images and images from sophisticated body-scanning devices. For remote sensing, the initial impetus was the program of unmanned planetary satellites in the 1960s that *telemetered* (transmitted) images to ground receiving stations. The low quality of the images required the development of processing techniques to make the images useful. Another impetus was the Landsat program, which began in 1972 and provided the first sets of worldwide imagery in digital format. A third impetus was and remains the continued development of faster, more powerful, and less expensive computer systems for image processing.

This chapter describes and illustrates the major categories of image processing. Jensen (1986) and Schowengerdt (1983) describe in detail the methods and the mathematical transformations.
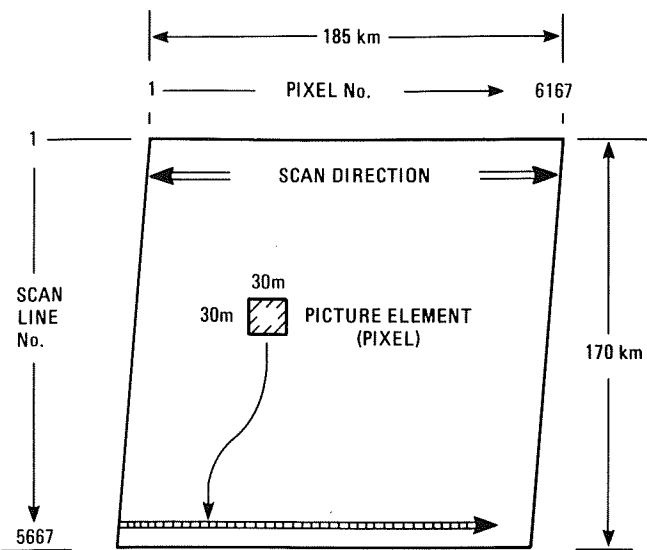
STRUCTURE OF DIGITAL IMAGES

One can think of any image as consisting of small, equal areas, or *picture elements*, arranged in regular rows and columns, called a *raster array*. The position of any picture element, or *pixel*, is determined on an *xy* coordinate system. Each pixel also has a numerical value, called a *digital number* (DN), that records the intensity of electromagnetic energy measured for the ground resolution cell represented by that pixel. Digital numbers range from zero to some higher number on a gray scale. This system records an image in strictly numerical terms on a three-coordinate system in which the *x*- and *y*-values locate each pixel and *z* gives the DN, which is displayed as a gray-scale intensity value. Scanner systems record images directly in a digital format where each ground resolution cell is represented by a pixel. Analog images, such as photographs and maps, may be converted into digital format by a process known as *digitization*. In this chapter digital image processing is largely illustrated using Landsat examples because the data are readily available and the images are familiar. The digital processes, however, are equally applicable to all forms of digital image data.

Landsat TM Images

Landsat TM data are available as *computer-compatible tapes* (CCTs) or as CD-ROMs, which can be read and processed by computers. Spectral bands and other characteristics of TM images are described in Chapter 3. Figure 8-1 illustrates the format of the digital data. The cross-track scanner has a ground resolution cell of 30 by 30 m. An oscillating scan mirror sweeps the cell alternately east and west across the terrain to produce scan lines oriented at right angles to the satellite orbit path. Scanning is continuous along the orbit; the data are subdivided into scenes consisting of 5667 scan lines that are 185 km long in the scan direction and 30 m wide in the orbit direction. The analog signal is sampled at intervals of 30 m to produce 6167 pixels (measuring 30 by 30 m) per scan line. Each TM image band consists of 34.9×10^6 pixels (Figure 8-1). The

Figure 8-1 Arrangement of scan lines and pixels in a Landsat TM image.

185 km / PIXEL No. 1 — 6167 / SCAN DIRECTION / SCAN LINE No. / 30m / 30m / PICTURE ELEMENT (PIXEL) / 170 km / 5667

5667 scan lines × 6167 pixels = 34.9 × 10⁶ pixels per band
34.9 × 10⁶ pixels × 7 bands = 244.3 × 10⁶ pixels per scene

seven bands have a total of 244.3×10^6 pixels. Each of the six TM visible and reflected IR bands employs an array of 16 detectors; each sweep of the scan mirror records 16 lines of data. The thermal IR band 6 employs four detectors with 120-by-120-m ground resolution cells; these are resampled to 30-by-30-m pixels. (*Note:* in CCTs produced by EOSAT through 1989, pixel size was 28.5 by 28.5 m.) TM data are recorded on an 8-bit scale. Bernstein and others (1984) have analyzed the performance of the TM system; NASA (1983) gives details of the CCT format for TM data.

The structure of a TM digital image is illustrated in Figure 8-2, which is a greatly enlarged portion of band 4 from the Thermopolis, Wyoming, subscene that was described in Chapter 3. Figure 8-2A shows an array of 66 by 66 pixels. Bright pixels have high DNs, and dark pixels have lower DNs. Figure 8-2B is a map that shows the location for the printout of DNs in Figure 8-2C. The correlation of the image gray scale to the 8-bit DN scale is shown in Figure 8-2D, where a DN of 0 is displayed as black and 255 as white. A *histogram* (Figure 8-2D) is a useful way to display the statistics of an image. The vertical scale records the number of pixels associated with each DN value, shown on horizontal scale.

Referring again to the printout (Figure 8-2C), note the low values associated with the Wind River and the high values of the adjacent vegetation. These values are consistent with the strong absorption by water and strong reflection by vegetation of the IR energy recorded by TM band 4. In the river, note that the lowest digital numbers (DN = 8 to 17) correspond to the

center of the stream; pixels along the stream margin have higher values (DN = 20 to 80). The 30-by-30-m ground resolution cells in the center of the river are wholly occupied by water, whereas marginal cells are occupied partly by water and partly by vegetation, resulting in a DN intermediate between water and vegetation. The mixed pixels form narrow gray bands along the river in Figure 8-2A. The TM format is typical of all multispectral digital data sets.

CCTs of Landsat images for the world are available from EOSAT at a cost of $4400 for a TM scene. CCTs are available as exabyte tape cartridges or as CD-ROMs. CCTs of TM images acquired from 1982 to 1986 are available from the EROS Data Center (EDC) for $650; these images are recorded as four quadrants that must be digitally mosaicked in order to process the entire scene. CCTs for MSS images are available from the EDC. TM images are indexed with the path-and-row system described in Chapter 3.

Digitization Procedure

Digitization is the process of converting an analog image into a raster array of pixels. Maps and other information may also be digitized. The digitized information is stored on a magnetic medium for subsequent computer processing. Digitizing systems belong to several categories: drum, flatbed, and linear array.

A typical *drum digitizing system* (Figure 8-3) consists of a rotating cylinder with a fixed shaft and a movable carriage that holds a light source and a detector similar to a photographic light meter. The positive or negative transparency is placed over the opening in the drum, and the carriage is positioned at a corner of the film. As the drum rotates, the detector measures intensity variations of the transmitted light caused by variations in film density. Each revolution of the drum records one scan line of data across the film. At the end of each revolution, the encoder signals the drive mechanism, which advances the carriage by the width of one scan line to begin the next revolution.

The width of the scan line is determined by the optical aperture of the detector, which typically is a square opening measuring 50 μm on a side. The analog electrical signal of the detector, which varies with film density changes, is sampled at 50-μm intervals along the scan line, digitized, and recorded as a DN value on magnetic tape. Each DN is recorded as a series of *bits*, which form an ordered sequence of ones and zeroes. Each bit represents an exponent of the base 2. The widely used 8-bit series represents 256 values on the gray scale ($2^8 = 256$ levels) with 0 for black and 255 for white. A group of 8 bits is called a *byte*. The film image is thus converted into a raster array of pixels that are referenced by scan-line number (*y*-coordinate) and pixel count along each line (*x*-coordinate). A typical black-and-white aerial photograph measuring 23 by 23 cm (9 by 9-in.) that is digitized with a 50-μm sampling interval is converted into 21.2 million pixels.
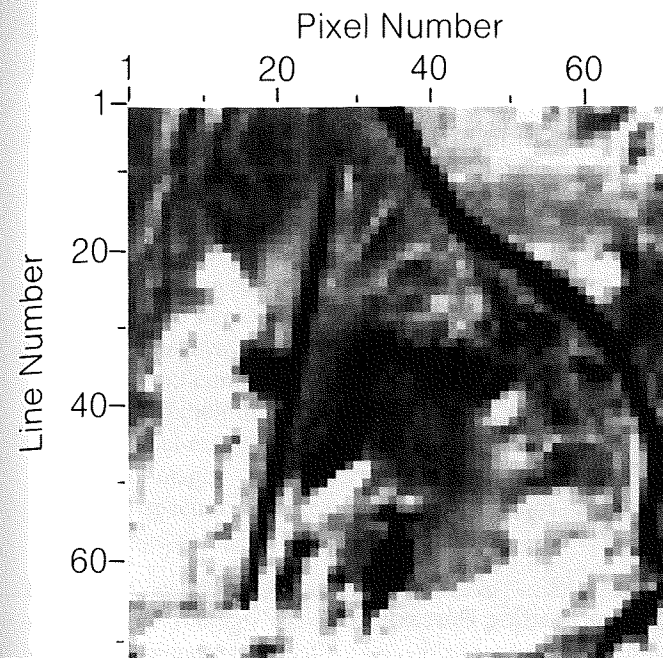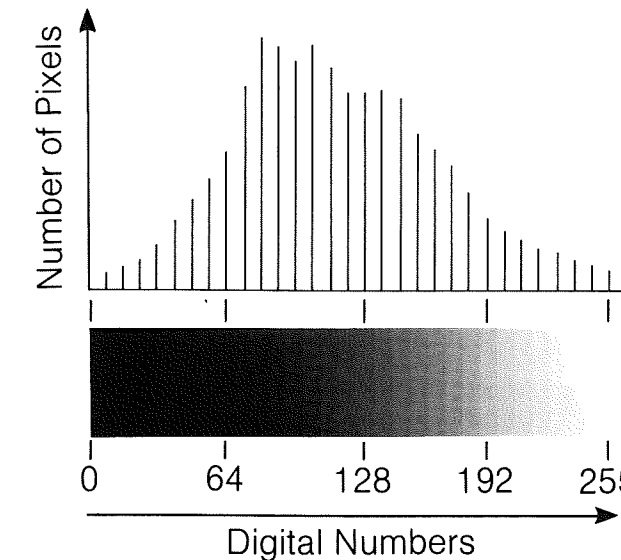

A. Gray-scale image.
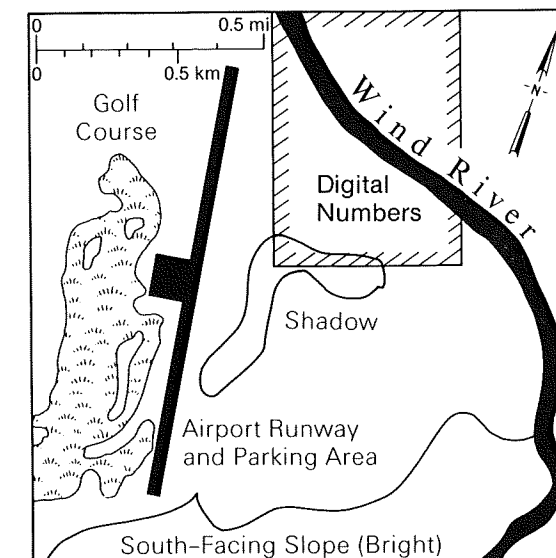
B. Location map.
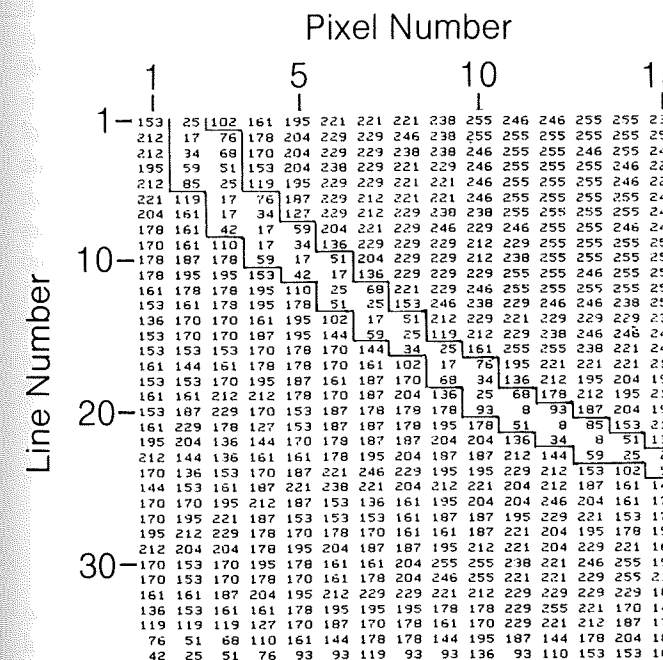
C. Array of DNs for the area shown in the location map.

D. Histogram and gray scale.

Figure 8-2 Digital structure of a Landsat TM band 4 image. The area is a portion of the Thermopolis, Wyoming, subscene shown in Chapter 3.

The intensity of the digitizer light source is calibrated at the beginning of each scan line to compensate for any fluctuations of the light source. These drum digitizers are fast, efficient, and relatively inexpensive. Color images may be digitized into the values of the component primary colors on three passes

through the system using blue, green, and red filters over the detector. A digital record is produced for each primary color, or wavelength band.

In *flatbed digitizers*, the film is mounted on a flat holder that moves in the *x* and *y* directions between a fixed light source
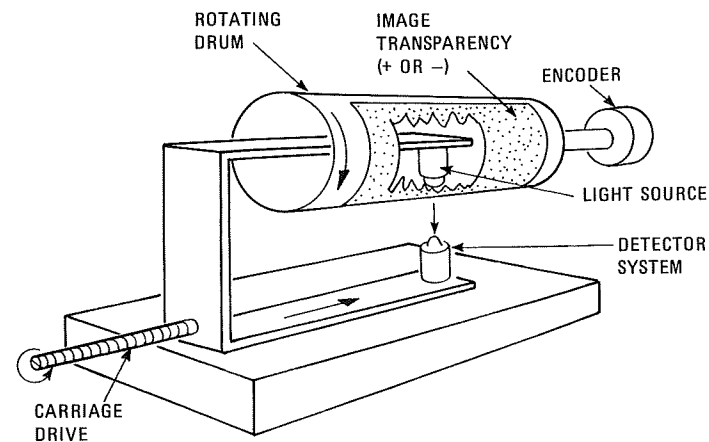
Figure 8-3 System for digitizing an analog image, such as a photograph. From Bryant (1974, Figure 2).

and a detector. These devices are usually slower and more expensive than drum digitizers, but they are also more precise. Some systems employ reflected light in order to digitize opaque paper prints. The resulting voltage signal for each line is digitized and recorded.

Linear-array digitizers are similar to the along-track scanners described in Chapter 1. An optical system projects the image of the original photograph onto the focal plane of the system. A mechanical transport system moves a linear array of detectors across the focal plane to record the original photograph in digital form.

The digitized image is recorded magnetically and can be read into a computer for various processing operations. The processed data are then displayed as an image on a viewing device or plotted onto film as described in the following section. Inexpensive small-format digitizers are available as accessories for personal computers.
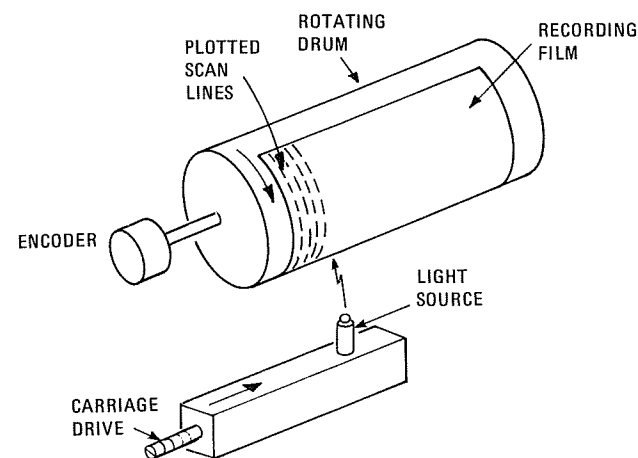

Figure 8-4 System for plotting an image from digital data. From Bryant (1974, Figure 3).

Image Plotting Procedure

Digital image data are plotted as images by *film writers* (Figure 8-4). Recording film is mounted on a rotating drum. With each rotation a scan line is exposed on the film by a light or laser, the intensity of which is modulated by the DNs of the pixels. On completion of each scan line, the carriage advances the light source to commence the next line. The exposed film is developed to produce a transparency from which one can make contact prints and enlargements. Modern plotters record data directly onto color film; three passes are made, each with a red, green, or blue filter over the light source. Advanced plotters mix the red, green, and blue components for each pixel and plot the color image in a single pass.

Color printers are available as accessories for personal computers and produce acceptable page-size prints. In order to produce high-quality prints of entire TM images at intermediate scales (1:250,000 or larger), film transparencies must be plotted and photographically enlarged.

IMAGE-PROCESSING OVERVIEW

Image-processing methods are grouped into three functional categories; these are defined next, together with lists of typical processing routines.

1. *Image restoration* compensates for data errors, noise, and geometric distortions introduced during the scanning, recording, and playback operations.
   a. Restoring line dropouts
   b. Restoring periodic line striping
   c. Restoring line offsets
   d. Filtering random noise
   e. Correcting for atmospheric scattering
   f. Correcting geometric distortions

2. *Image enhancement* alters the visual impact that the image has on the interpreter in a fashion that improves the information content.
   a. Contrast enhancement
   b. Density slicing
   c. Edge enhancement
   d. Making digital mosaics
   e. Intensity, hue, and saturation transformations
   f. Merging data sets
   g. Synthetic stereo images

3. *Information extraction* utilizes the decision-making capability of the computer to recognize and classify pixels on the basis of their digital signatures.
   a. Principal-component images
   b. Ratio images
   c. Multispectral classification
   d. Change-detection images

These routines are described and illustrated in the following sections. The routines are illustrated with Landsat examples, but the techniques are equally applicable to other digital image data sets. A number of additional routines are described in the reference publications.

IMAGE RESTORATION

Restoration processes correct the errors, noise, and geometric distortion introduced into the data during the scanning, transmission, and recording of images. The objective is to make the image resemble the original scene. In the early days of Landsat (mid-1970s) defects were not uncommon. Today, however, defects are relatively rare. For most TM centerpoints there are enough repeated images available that users can avoid defective data sets. Image restoration is relatively simple because the pixels from each band are processed separately.
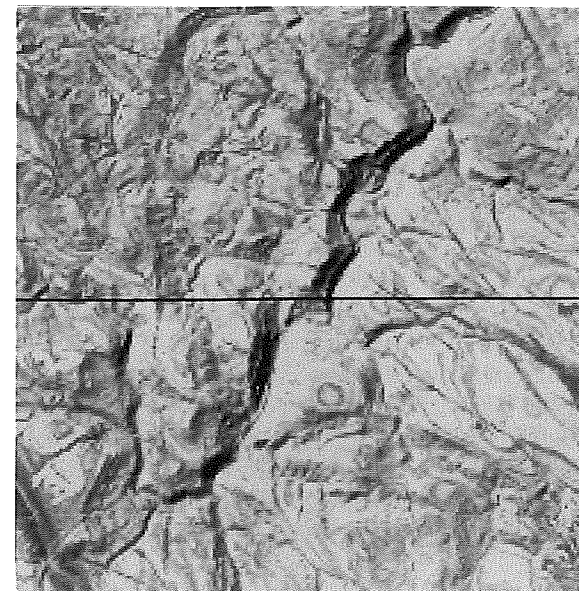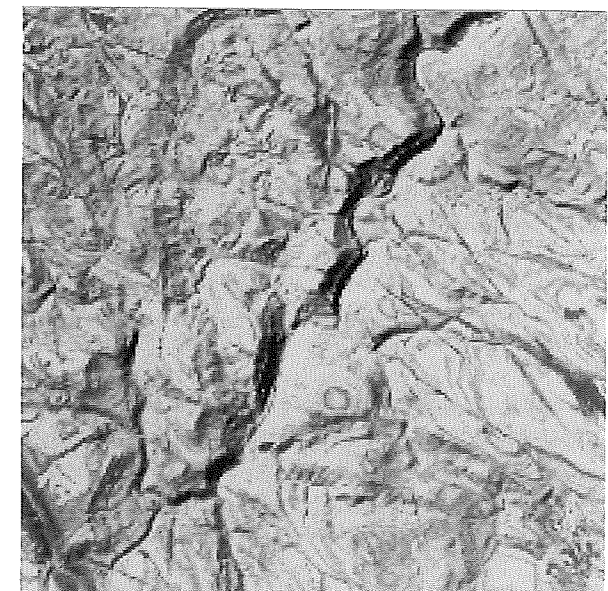
Restoring Line Dropouts

The image in Figure 8-5A has a line dropout, which is a black scan line caused by a missing line of data; the resulting string of zero DNs produces the black line. The defect is restored by replacing each value of DN 0 with a DN calculated as the average of the DN values for the adjacent pixel in the nondefective scan lines that precede and succeed the missing line. Figure 8-5B shows the restored image.
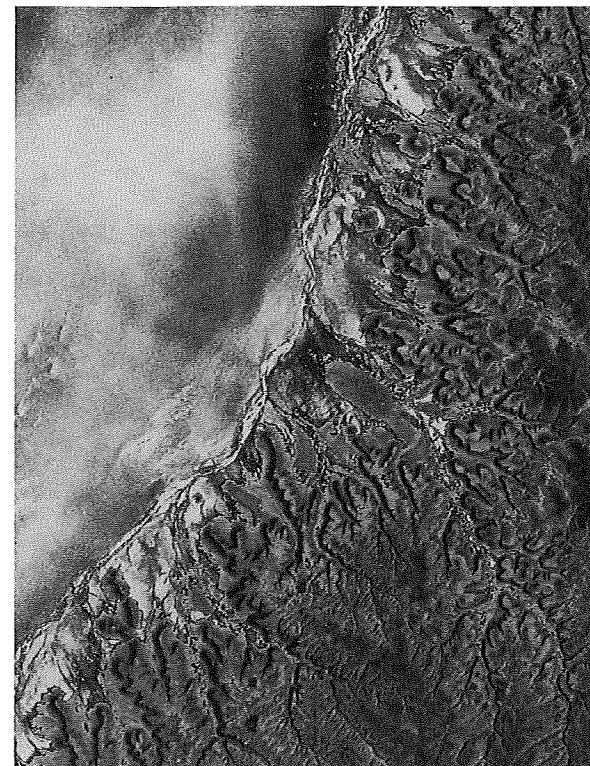
Restoring Banding

Each eastbound and westbound sweep of the TM scan mirror acquires 16 scan lines for the detector arrays for each band. On some images the average brightness for the eastbound lines differs from the westbound lines, which causes alternating brighter and darker bands that are 16 scan lines wide. Figure 8-6A shows this defect, which is called *banding*. The banding is most apparent in uniform stretches of terrain such as water or desert. Restoration programs calculate the average histograms for the brighter and darker bands. The histograms are then adjusted to a uniform average brightness level for both sets of scan lines. Figure 8-6B shows the restored image.

Restoring Line Offsets

Figure 8-7A shows an uncommon but deleterious defect called *line offsets,* in which individual scan lines are offset east or west from their correct position. In Figure 8-7A lines are offset to the west, causing bright lines of land signatures to appear in the dark ocean. At first glance this image looked hopeless. Careful analysis of the digital data file showed that the defects could be restored. Each scan line should begin at pixel reference 1 on the west margin of the image, as shown in Figure 8-2C. The defective scan lines, however, originated at higher pixel numbers, which caused the offset on the image.

A. Original image with line dropout.

B. Restored image.

Figure 8-5 Restoring line dropouts on a Landsat TM image of central Yemen.

A. Original image with banding.

B. Restored image.

Figure 8-6 Restoring banding on a Landsat TM image of the Red Sea coast of Yemen.

A. Original image with line offsets.

B. Restored image.

Figure 8-7 Restoring offset scan lines. Landsat TM band 4 image of Oxnard, California.

The higher initial pixel numbers were corrected to 1, and the restored image in Figure 8-7B was generated.

Filtering of Random Noise

Nonrandom defects, such as banding, are readily recognized and restored by simple means. Random defects, on the other hand, require more sophisticated restoration methods. One random defect occurs as individual pixels with DNs that are much higher or lower than the surrounding pixels. These pixels produce scattered bright and dark specks called *random noise,*

which mar the image. These specks also interfere with information-extraction procedures such as classification. Random-noise pixels are removed by digital filters.

Figure 8-8A shows an array of Landsat pixels, most of which have DN values ranging from 40 to 60. There are, however, two pixels with DN values of 0 and 90 that produce dark and bright noise in the image. This noise may be eliminated by applying a *moving average filter* in the following steps:

1. Design a *filter kernel*, which is a two-dimensional array of pixels with an odd number of pixels in both the x and y dimensions. The odd-number requirement means that the kernel has a central pixel, which will be modified by the filter operation. In Figure 8-8A, a 3-by-3 kernel is shown by the outlined box.
2. Calculate the average of the 9 pixels in the kernel; for the initial location, the average is 43.
3. Determine the difference between the average value and the central pixel ($43 - 0 = 43$).
4. If the difference exceeds (+ or –) a threshold value, in this example 20, replace the central pixel with the average value. In Figure 8-8B the original central pixel with a value of 0 has been replaced by 43.
5. Move the kernel to the right by one column of pixels, and repeat the operation. The new average is 50. The central pixel (40) is within the threshold limit of the new average and remains unchanged. In the third position of the kernel, the central pixel (DN = 90) is replaced by the average (53).
6. When the right margin of the kernel reaches the right margin of the pixel array, the kernel returns to the left margin, drops down one row of pixels, and the operation continues until the entire image has been subjected to the moving average filter.

Moving average filters are widely used in other image-processing applications.

Correcting for Atmospheric Scattering

Chapter 2 described how the atmosphere selectively scatters the shorter wavelengths of light, which causes haze and reduces the contrast ratio of images. For TM images, band 1 (blue) has the highest component of scattered light and band 7 (reflected IR) has the least. Figure 8-9 shows two techniques for determining the correction factor for different TM bands. Both techniques are based on the fact that band 7 is essentially free of atmospheric scattering, which can be verified by examining the DNs for shadows; these have values of either 0 or 1 on band 7. The first technique (Figure 8-9A) employs an area within the image that has shadows caused by irregular topography. For each pixel the DN in band 7 is plotted against the DN in band 1, and a straight line is fitted through the plot, using a least-squares technique. If there were no haze in band 1, the line would pass through the origin. Because there is haze, the

Average values
for successive
3 by 3 pixel kernels
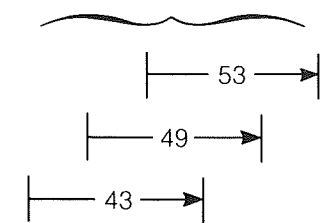
A. Original data with filter kernel (3 by 3 pixels).

B. Filtered data with noise pixels replaced by average values, shown in circles.

**Figure 8-8** Filtering to remove random-noise pixels.

intercept is offset along the band 1 axis, as shown in Figure 8-9A. Haze has an additive effect on scene brightness. To correct the haze effect on band 1, the value of the intercept offset is subtracted from the DN of each band 1 pixel for the entire image. The procedure is repeated for the other TM bands.

Figure 8-9B shows a second restoration technique which also requires that the image have some shadows or other areas with DNs of 0 on band 7. The histogram of band 7 (Figure 8-9B) has pixels with DNs of 0. The histogram of band 1 lacks pixels in the range from 0 to approximately 20 because of light scattered into the detector by the atmosphere. The band 1 histogram also shows the characteristic, abrupt increase in pixels at a DN of approximately 20. This value of 20 is subtracted from all the DNs in band 1 to restore the effects of atmospheric scattering. The histograms of bands 2 and 3 are also restored in this manner. Band 2 (green) normally requires a subtraction of less than 10 DNs. Only a few DNs are typically subtracted from band 3 (red).

The amount of atmospheric correction depends upon wavelength of the bands and the atmospheric conditions. As mentioned earlier, scattering is more severe at shorter wavelengths. Humid, smoggy, and dusty atmospheres cause more scattering than clear, dry atmospheres.
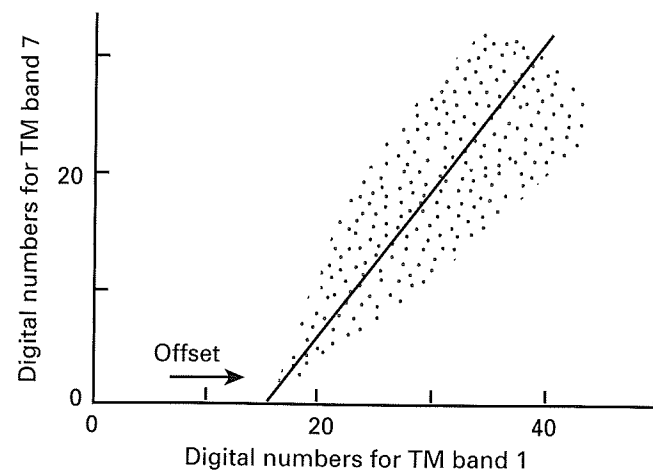
A. Plot of TM band 7 versus band 1 for an area with shadows. Offset of the line of least-squares fit along band 1 axis is caused by atmospheric scattering in that band.
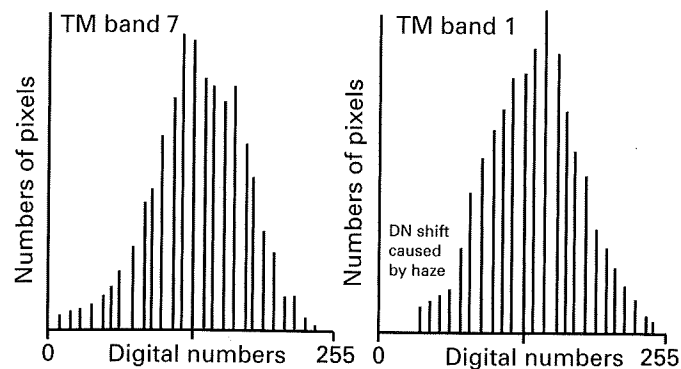
B. Histograms for TM bands 7 and 1. The lack of pixels with low DNs in band 1 is caused by illumination from light selectively scattered by the atmosphere.

Figure 8-9 Methods for determining atmospheric corrections on individual TM bands. From Chavez (1975, Figures 2 and 3).

Geometric Restorations

The scanning of TM images introduces a number of geometric irregularities that are classified as systematic and nonsystematic distortions. After these distortions are restored, the image may be rectified to match a specific map format.

Nonsystematic Distortions *Nonsystematic distortions* (Figure 8-10A) are caused by variations in the spacecraft attitude, velocity, and altitude and therefore are not predictable. These distortions must be evaluated from Landsat tracking data or ground-control information. Variations in spacecraft velocity cause distortion in the along-track direction only and are known functions of velocity that can be obtained from

tracking data. The amount of earth rotation during the 26 sec required to scan a TM image results in distortion in the scan direction that is a function of spacecraft latitude and orbit. In the correction process, successive groups of 16 scan lines are offset toward the west to compensate for earth rotation, which causes the parallelogram outline of the restored image.

Variations in attitude (roll, pitch, and yaw) and altitude of the spacecraft cause nonsystematic distortions that must be determined for each image in order to be corrected. The correction process employs geographic features on the image, called *ground control points* (GCPs), whose positions are known. Intersections of major streams, highways, and airport runways are typical GCPs. Latitude and longitude of GCPs may be determined from accurate base maps. Where maps are lacking we use portable devices called *gobal positioning systems* (GPSs) that determine latitude and longitude from *navigation satellites* (Leick, 1995). The user locates a GCP in the field and determines its position using the GPS. Differences between actual GCP locations and their positions in the image are used to determine the geometric transformations required to restore the image. The original pixels are resampled to match the correct geometric coordinates. The various resampling methods are described by Rifman (1973), Goetz and others (1975), and Bernstein and Ferneyhough (1975).
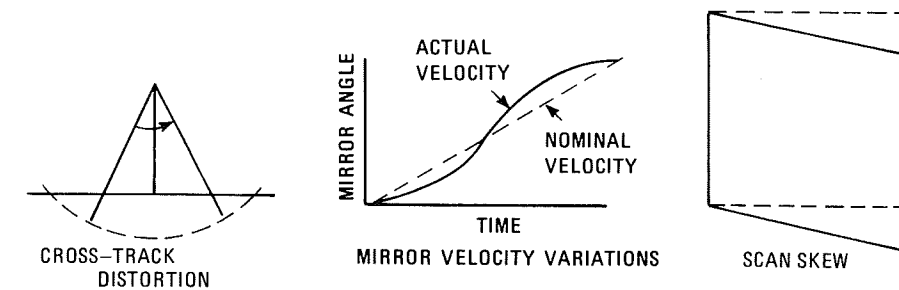
Systematic Distortions Geometric distortions whose effects are constant and can be predicted in advance are called *systematic distortions*. Scan skew, variations in scanner mirror velocity, and cross-track distortion belong to this category (Figure 8-10B). *Scan skew* is caused by the forward motion of the spacecraft during the time required for each mirror sweep. The ground swath scanned is not normal to the ground track but is slightly skewed, producing distortion across the scan line. The known velocity of the satellite is used to restore the correct geometric relationship.

Tests before Landsat was launched determined that the velocity of the scan mirror was not constant from start to finish of each scan line, resulting in minor systematic distortion along each scan line. The known mirror velocity variations are used to correct for this effect.

Cross-track distortion results from sampling pixels along a scan line at constant time intervals. The width of a pixel (in the scan direction) is proportional to the tangent of the scan angle and therefore is wider at either margin of the scan line. The data are recorded and displayed at a constant rate, however, which causes the pixels at margins of the image to be compressed relative to those at the center. Cross-track distortion occurs in all unrestored images acquired by cross-track scanners, whether from aircraft or satellites. Figure 8-11A is an original aircraft scanner image with cross-track distortion, which causes straight roads to be curved at the compressed margins. Figure 8-11C shows the constant width of the distorted pixels. Figure 8-11B is the image that was restored using trigonometric functions. Figure 8-11D shows the marginal
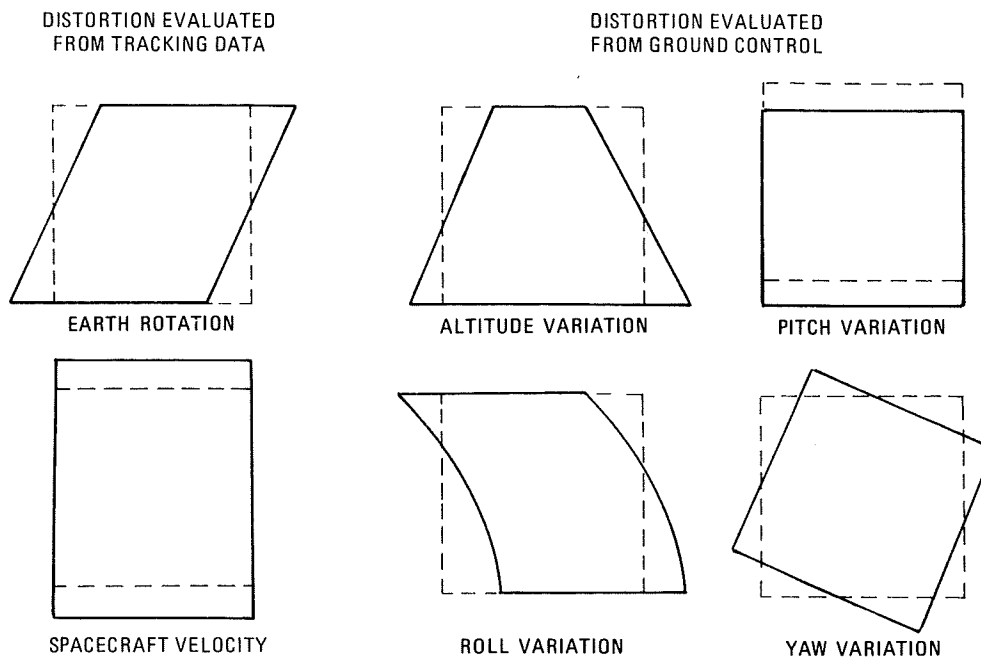
A. Nonsystematic distortions. Dashed lines indicate shape of distorted image. Solid lines indicate shape of restored image.

B. Systematic distortions.

Figure 8-10 Geometric distortions of Landsat images. From Bernstein and Fernyhough (1975, Figure 3).

pixels plotted at greater widths than central pixels, which restores the geometry. Distortion is pronounced in this aircraft image, which was recorded with a 90° scan angle. Distortion is less pronounced in TM images that are recorded with a 14.9° scan angle. Nevertheless, cross-track distortion is present and must be restored to have an undistorted TM image.

For Landsat and other satellite images the systematic distortions are corrected before the data are distributed.

Map and Image Projections

Images and maps contain inherent geometric distortions because they record the curved surface of the earth on a flat display. Areas, distances, and angular relationships are distorted to varying degrees. A *map projection* is the systematic represen-

tation of a curved surface on a plane. Figure 8-12 shows the three basic projections, which are planar, conic, and cylindrical. The conic and cylindrical projections are "unrolled" into flat surfaces. Many different versions of the basic projections have been devised for different purposes. The history, characteristics, and mathematics of map projections are given by Snyder (1987), which forms the basis for the following discussion. The cylindrical projection is developed by unrolling a cylinder wrapped around the globe, touching at a great circle, with meridians projected from the center of the globe.

Mercator Projections A well-known type of cylindrical projection is the *Mercator projection,* which is also important because it has similar characteristics to images acquired by Landsat. A Mercator projection has the following characteristics:
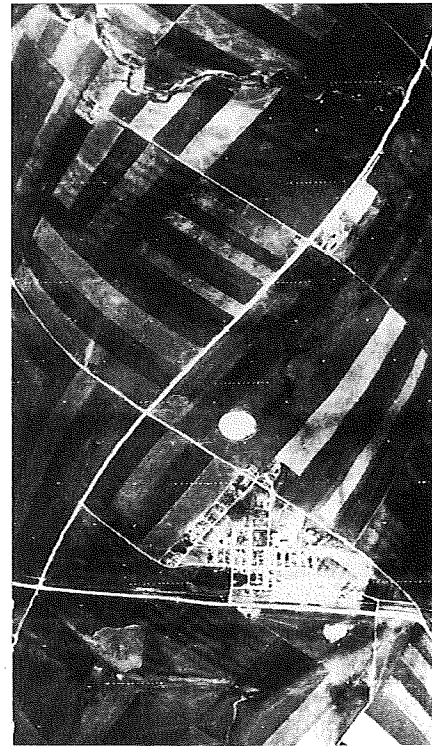
A. Original distorted image.
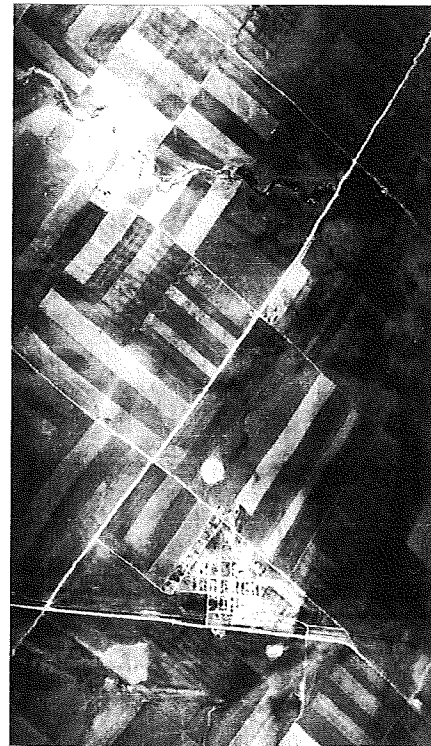
B. Restored image.

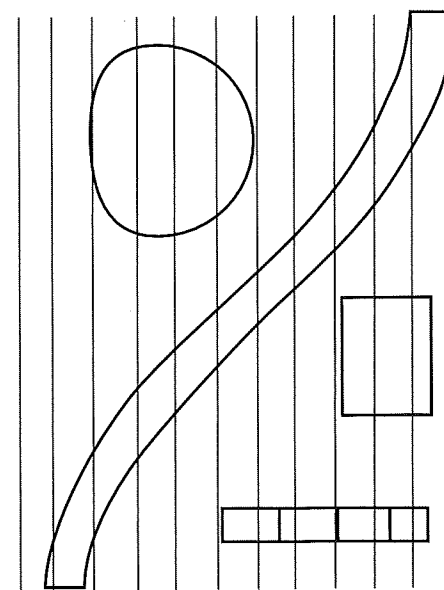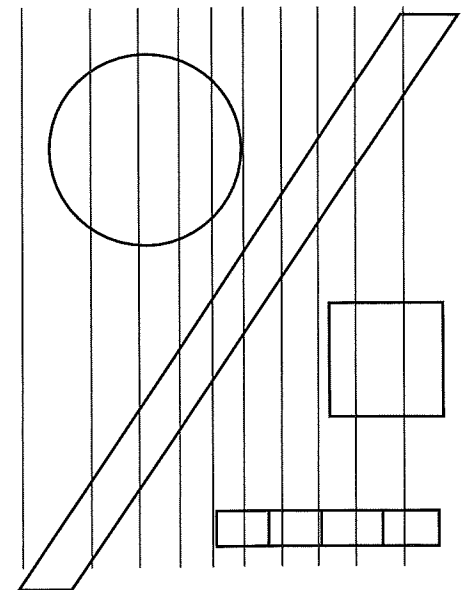

C. Geometry of distorted image.

D. Geometry of restored image.

Figure 8-11 Cross-track distortion and restoration on images.
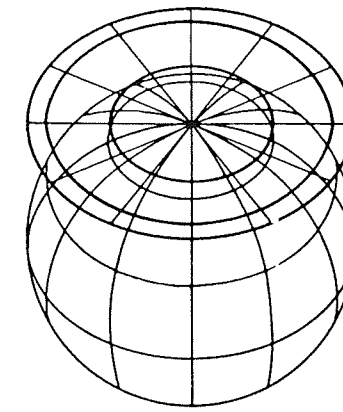
A. Polar azimuthal (Planar).
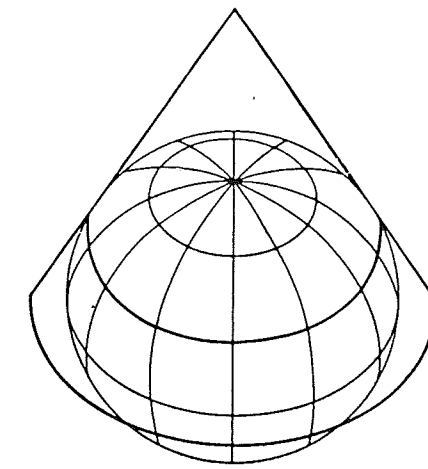
B. Regular conic.
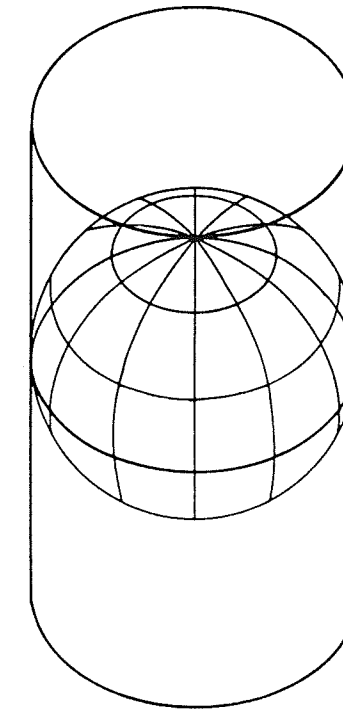
C. Regular cylindrical (Mercator).
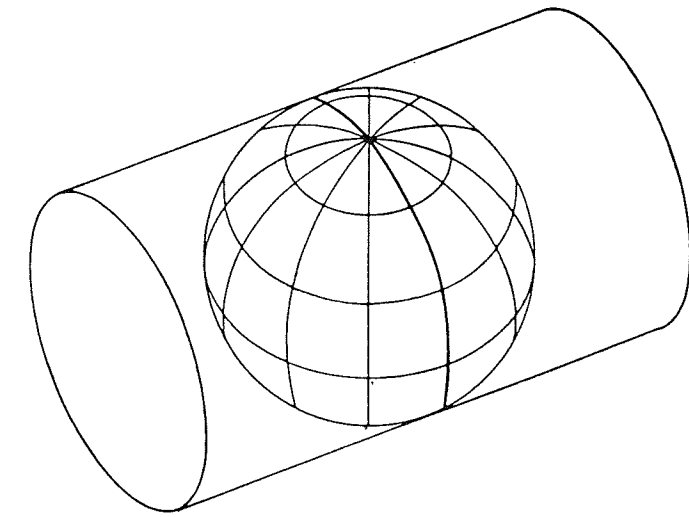
D. Transverse cylindrical (Transverse Mercator).

Figure 8-12 Basic map projections. From Snyder (1987, Figure 1).

1. The great circle of contact with the cylinder is the equator, as shown in Figure 8-12C.
2. Maps are *conformal;* that is, the relative local angles about every point are shown correctly. Although the shape of a large area is distorted, its small features are shaped essentially correctly.
3. Meridians are equally spaced parallel lines; parallels are unequally spaced parallel lines.
4. There is little error close to the equator. (The scale 10° north or south is only 1.5 percent larger than at the equator.)

Because of these useful attributes, other versions of the Mercator projection have been developed. In the *Transverse Mercator projection* the cylinder is oriented at a right angle to the equator. The great circle, of contact, is a longitude line called the central meridian. Map scale is essentially true within a zone 10° east or west of the central meridian. The most widely used maps are based on the *Universal Transverse Mercator* (UTM) projection in which the earth, between latitudes 84°N and 80°S, is divided into 60 zones, each generally 6° wide in latitude. Each zone is divided into 20 quadrangles

generally 8° high in latitude. Each quadrangle is divided into grid squares 10,000 m on a side. Locations are readily identified by referring to the grid coordinates. Snyder (1987) provides additional information on the UTM projection.

Space Oblique Projection Landsat and similar polar-orbiting satellites acquire images in the *Space Oblique Mercator* (SOM) projection, which is a version of the transverse mercator projection. Figure 8-13 shows the SOM in which the cylinder is tangential to a great circle formed by the satellite ground track. The 185-km width of the image swath is determined by the angular field of view of the scanner and the altitude of the satellite. The scanning is a continuous process; the image swath is divided into individual TM scenes at intervals of 170 km along the orbit path (Figure 8-13). TM images are conformal and essentially true to scale throughout. The scale at the east and west margins averages 0.015 percent greater than along the central orbit track (Snyder, 1987).

Some users need images displayed in different projections. *Rectification* is the process of converting an image into a specified projection. Rectification employs GCPs (described in the section "Nonsystematic Distortions"), which are identified on the image and assigned latitude and longitude coordinates from existing maps or from GPS information. The computer program then resamples the original image pixels into the specified map projection.

For most uses images must be annotated with latitude and longitude coordinates and/or a UTM grid. The annotations may be added during the rectification process. If images are not rectified, the coordinates may be added to the original SOM projection by using GCPs. My associates routinely use annotated TM images (1:50,000 and 1:100,000 scale) for mineral exploration in Mexico and South America. Portable GPS receivers determine actual ground positions, which are compared with positions from the UTM grid on the images. The positions typically match within 100 m, which is suitable for much fieldwork.

IMAGE ENHANCEMENT

Enhancement is the modification of an image to alter its impact on the viewer. Generally, enhancement changes the original digital values; therefore, enhancement is not done until the restoration processes are completed.

Contrast Enhancement

Contrast enhancement modifies the gray scale to produce a more interpretable image. Virtually all bands of all images acquired by Landsat (and similar satellites) require contrast enhancement. Figure 8-14A is a TM band 4 image of the Thermopolis subscene that was plotted directly from the CCT. These original unenhanced images are sometimes called *raw*
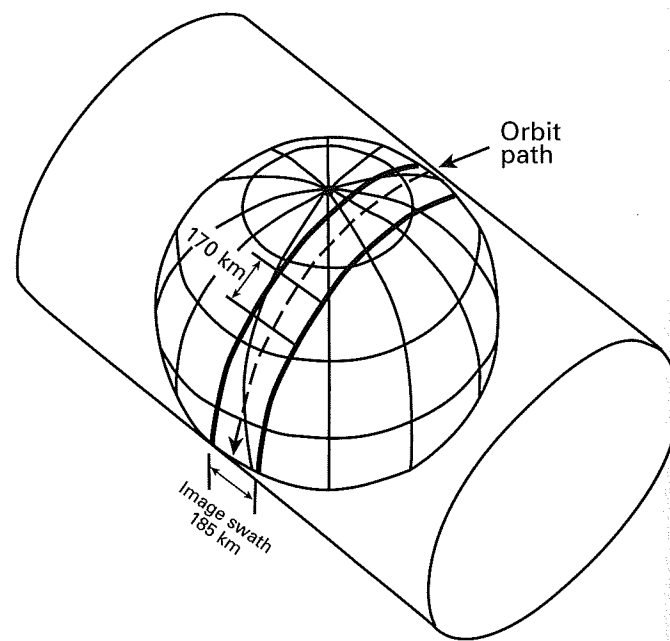

Figure 8-13 Space Oblique Mercator projection of Landsat images.

images. The image is very dark and lacks contrast. The histogram (Figure 8-14B) shows the statistical distribution of the raw data. The median value is 30, which explains the dark appearance of the image. The data occupy a limited range from 0 to 65. This range is only 25 percent of the TM system range (0 to 255) and explains the low contrast of the image.

The image in Figure 8-14A is representative of virtually all raw TM images. Contrary to appearances, the characteristics of raw images do not indicate a defect in the TM system. The sensitivity range of TM detectors was designed to record a wide range of terrain brightness from black basalt plateaus to white sea ice under a wide range of lighting conditions. No individual scene has a brightness range that covers the full sensitivity range of the TM detectors. Therefore, each original TM band requires contrast enhancement to produce useful images. Contrast enhancement is a subjective operation that can be strongly influenced by personal preferences of the operator and user. Histograms of the enhanced data give an objective view of the process. Many routines have been developed for enhancing contrast; three useful methods are described in the following sections.

Linear Contrast Stretch All contrast stretches are done with *lookup tables (*LUTs*)*, which consist of an array of original (*input*) pixel values and a corresponding array of enhanced (*output*) values that are used to produce the stretched image. Figure 8-15 is a graphic display of an LUT that was used to enhance the original data shown in the histogram of Figure 8-14B. The vertical axis represents the original pixels, and the

horizontal axis represents the enhanced pixels. The scale of the input axis is twice that of the output axis. The heavy solid and dashed lines show the enhancement transforms. In a simple (unsaturated) linear contrast stretch, the lowest original DN is assigned a new value of 0, the highest original DN is assigned a new value of 255, and the remaining original DNs are linearly reassigned new values ranging from 1 to 254. A disadvantage of this stretch is that the few percent of original pixels at the head and tail of the original histogram occupy an excessive portion of the new dynamic range.

This disadvantage is eliminated with the *saturated contrast stretch* shown by the solid line in the LUT (Figure 8-15). The darkest 2 percent (DN = 0 to 15) and brightest 2 percent (DN = 50 to 65) of the original input pixels are assigned output values of 0 and 255; in other words, they are *saturated* to pure black and white. The remaining 96 percent of input pixels (DN = 16 to 49) are linearly reassigned to the output range from 1 to 254. The resulting output image and histogram are shown in Figure 8-14C,D. The dramatic impact of contrast enhancement is emphasized by comparing the output image (Figure 8-14C) with the input image (Figure 8-14A). For this example, a saturation of 2 percent was selected as optimum after experimenting with other saturation levels. Other images may require higher or lower saturation levels.

The following sections illustrate other commonly used contrast enhancements.

Gaussian Contrast Stretch Variations in nature are commonly distributed in a normal (Gaussian) pattern, which is the familiar bell-shaped curve. This distribution is emulated for images by the *Gaussian contrast stretch,* in which the original pixels are reassigned to fit a Gaussian distribution curve. The image and histogram in Figure 8-14E,F show the effect of applying a Gaussian stretch to the original data.

Uniform Distribution Contrast Stretch A *bin* of pixels refers to all pixels having the same DN. The linear and Gaussian stretches assign each bin of pixels to a uniform new DN range regardless of the number of pixels in the bin. For example, in the linear and Gaussian histograms the raw pixels with DN 20 and DN 30 are both given a uniform dynamic range, although the 30 bin contains 100 times more pixels. This disparity is compensated for in the *uniform distribution stretch* (or *histogram equalization stretch*), in which the input pixels are redistributed to produce a uniform population density of pixels along the output axis. The resulting output histogram (Figure 8-14H) has a wide spacing of bins in the center of the distribution curve and a close spacing of the less-populated bins at the head and tail of the histogram. In the resulting image (Figure 8-14G) the greatest contrast enhancement is applied to the most populated central range of DNs in the original image. Gray-level variations at the bright and dark extremes are compressed and become less distinct.

Other Contrast Stretches In addition to the standard methods described above, most software packages for image processing provide additional methods, such as exponential and logarithmic stretches. The user can also define custom contrast stretches. For example, TM images along the Red Sea coast include water (dark DNs), bedrock (intermediate DNs), and sand (bright DNs). An investigator who is interested in both water and sand could employ a custom stretch that assigns the dark half of the output DN range to water and the bright half to sand.

An important step in the process of contrast enhancement is for the user to inspect the original histogram and determine the elements of the scene that are of greatest interest. The user then chooses the optimum stretch for his or her needs. Experienced operators of image-processing systems bypass the histogram examination stage and interactively adjust the brightness and contrast of images that are displayed on a CRT. For some scenes a variety of stretched images are required to display fully the original data. It also bears repeating that contrast enhancement should not be done until other processing is completed, because the stretching modifies the original values of the pixels.

Density Slicing

Density slicing converts the continuous gray tone of an image into a series of density intervals, or slices, each corresponding to a specified range of DNs. Each digital slice is displayed as a separate color or outlined by contour lines. Qualitative analog displays are thus converted into quantitative digital displays, assuming that calibration data are available This technique also emphasizes subtle gray-scale differences that may be imperceptible to the viewer. Plate 9A is a density-sliced version of a black-and-white thermal IR image. The original continuous gray tones are shown in colors that represent discrete temperature ranges.

Edge Enhancement

Many interpreters are concerned with recognizing linear features in images. Geologists map faults, joints, and lineaments. Geographers map man-made linear features such as highways and canals. Some linear features occur as narrow lines against a background of contrasting brightness; others are the linear contact between adjacent areas of different brightness. In all cases, linear features are formed by edges. Some edges are marked by pronounced differences in brightness and are readily recognized. Typically, however, edges are marked by subtle brightness differences that may be difficult to recognize. *Edge enhancement* is the process of emphasizing the signatures of edges on images. Edges are enhanced in two ways:

1. Expanding the width of the linear feature
2. Increasing the DN difference across the feature

Two categories of digital filters are used for edge enhancement: directional filters and nondirectional filters.

A. Image from original data.
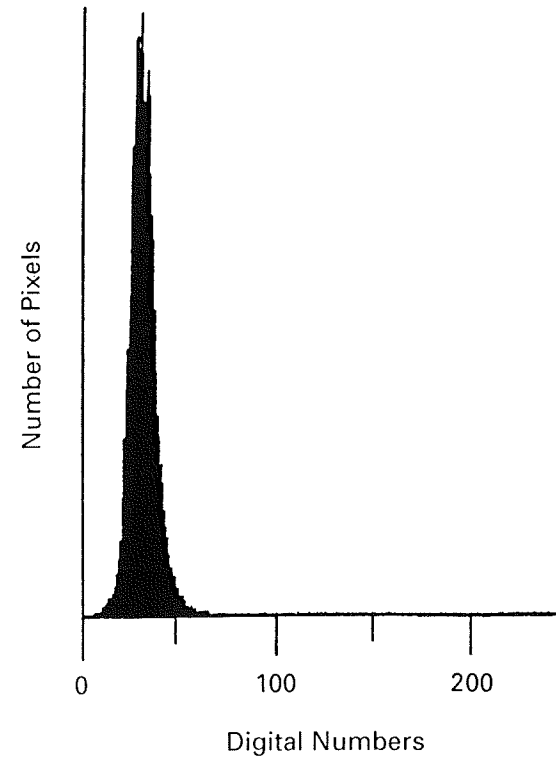
B. Histogram of original data.

E. Image with Gaussian contrast stretch.

F. Histogram of Gaussian contrast stretch.
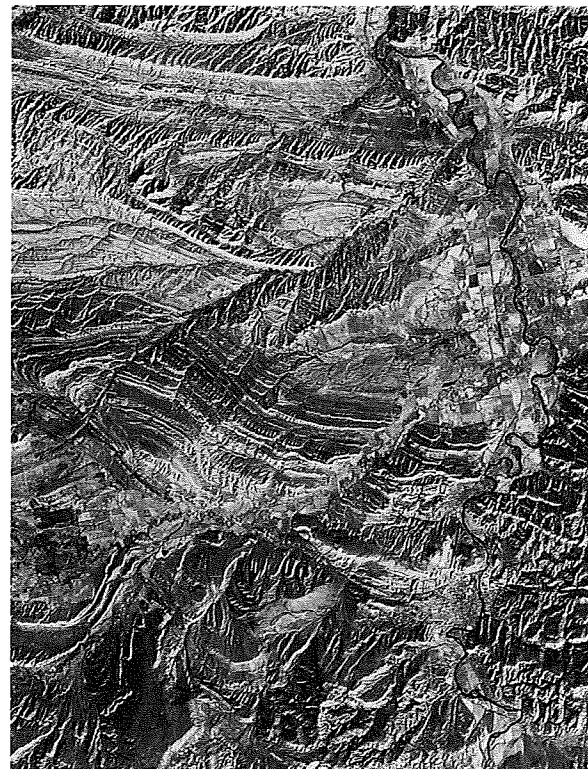
C. Image with linear contrast stretch and 2 percent saturation.

SATURATED
DARK 2%
OF PIXELS

SATURATED
BRIGHT 2%
OF PIXELS
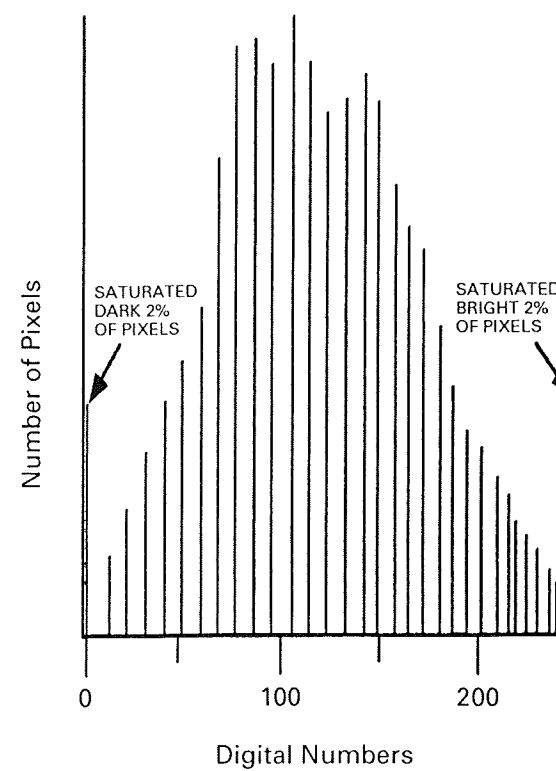
D. Histogram of linear contrast stretch and 2 percent saturation.
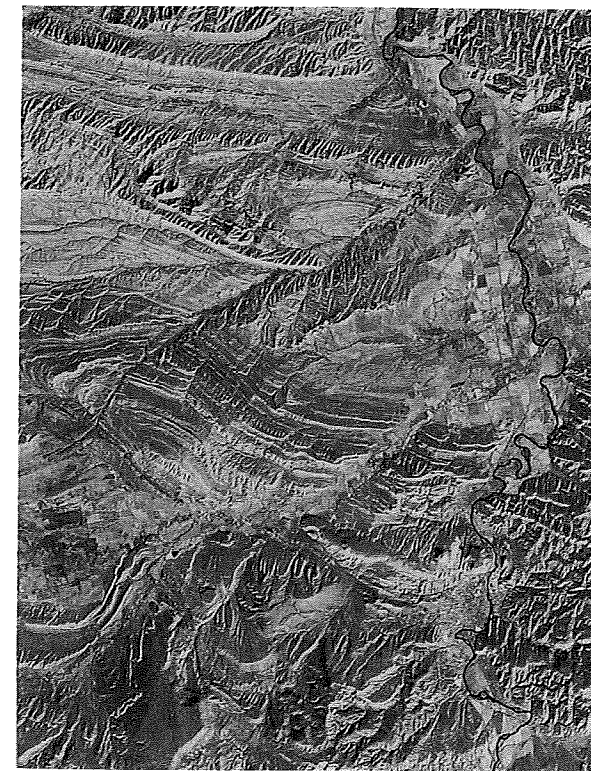
G. Image with uniform distribution stretch.
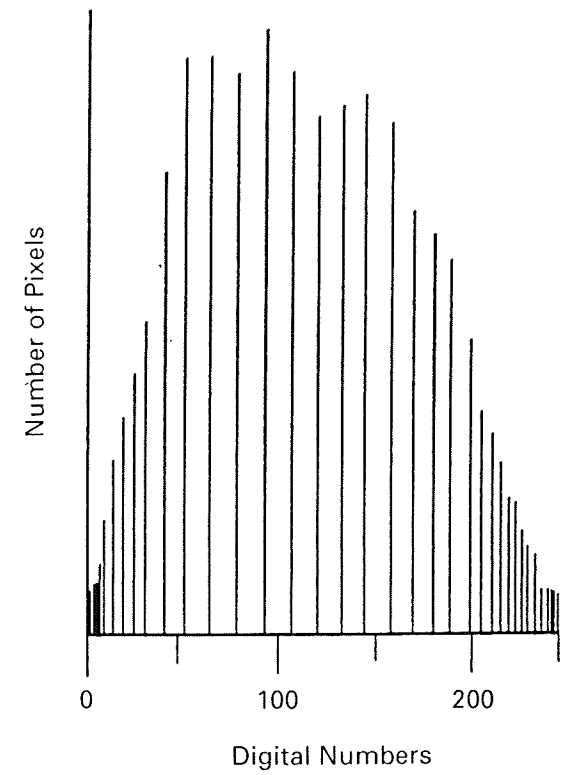
H. Histogram of uniform distribution stretch.

Figure 8-14 Contrast-enhancement methods. Landsat TM band 4 of the Thermopolis, Wyoming, subscene.

Figure 8-15 Graphic plot of the lookup table for a linear contrast stretch with 2 percent saturation.

Nondirectional Filters *Nondirectional filters* (also called *Laplacian filters*) are named because they have no directional bias in enhancing linear features; almost all directions are enhanced. The only exception applies to linear features oriented parallel with the direction of filter movement; these features are not enhanced. Figure 8-16A shows a Laplacian filter that is a kernel of three lines and three pixels. The kernel is a template with 4 as the central value, 0 at each corner, and −1 at the center of each edge. The Laplacian kernel is placed over a 3-by-3 array of original pixels (Figure 8-16A), and each pixel is multiplied by the corresponding value in the kernel. The nine resulting values (four of which are 0 and four are negative numbers) are summed. The resulting value for the filter kernel is combined with the original central pixel of the 3-by-3 data array, and this new number replaces the original DN of the central pixel. For example, consider the Laplacian kernel placed over the array of 3-by-3 original pixels indicated by the box in Figure 8-16A. When the multiplication and summation are performed, the value for the filter kernel is 5. The original central pixel in the array (DN = 40) is combined with the filter

A. Original image with DNs.

B. Enhanced by the factor 2.0.

C. Enhanced by the factor 5.0.

D. Enhanced by the factor 10.0.

Figure 8-17 Computer-generated images illustrating nondirectional edge enhancement with a Laplacian filter and different weighting factors.
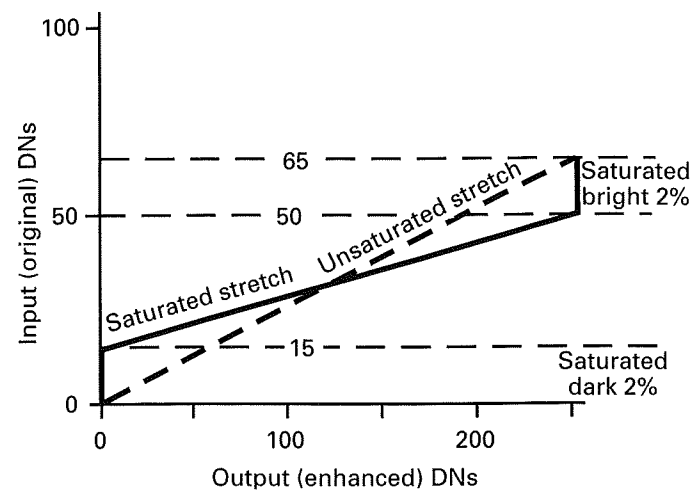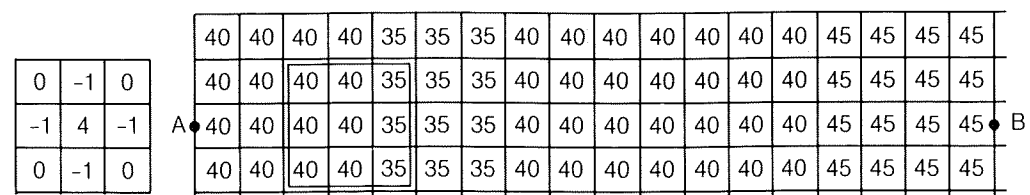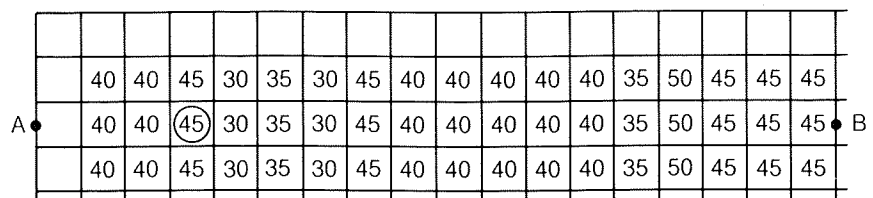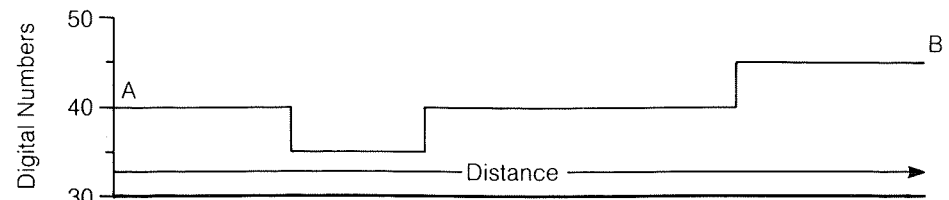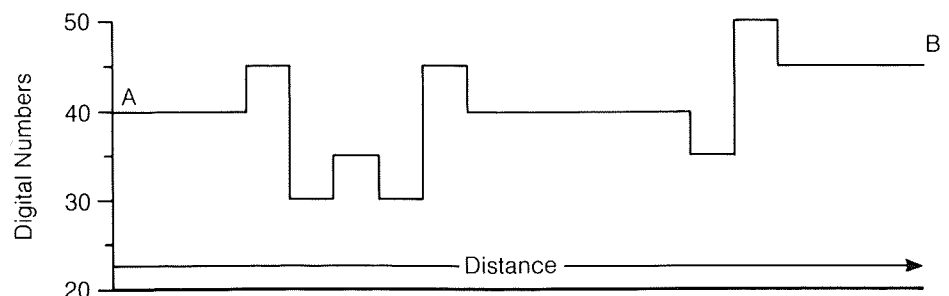

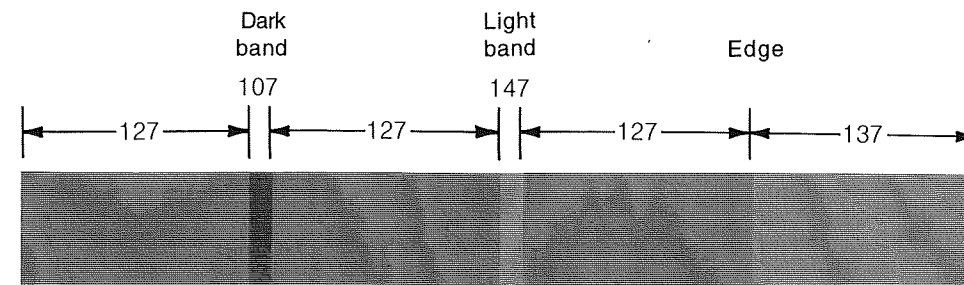A. Original data and Laplacian filter kernel.

B. Enhanced data.

C. Profile of the original data.

D. Profile of the enhanced data.

Figure 8-16 Nondirectional edge enhancement using a Laplacian filter.

value to produce the new value of 45, which is used in the filtered data set (Figure 8-16B). The kernel moves one column of pixels to the right, and the process repeats until the kernel reaches the right margin of the pixel array. The kernel then shifts back to the left margin, drops down one line of pixels, and continues the same process. Figure 8-16B shows the enhanced pixels. The outermost column and line of pixels are blank because they cannot form central pixels in an array.

The effect of the edge-enhancement operation can be evaluated by comparing profiles A–B of the original and the filtered data. Figure 8-16C is a profile of the original data. The regional background (DN = 40) is intersected by a darker lineament (DN = 35) that is three pixels wide and has DN values of 35. The contrast ratio between the lineament and background, as calculated from Equation (1-3), is 40/35, or 1.14. In the profile of the enhanced data (Figure 8-16D), the contrast ratio is 45/30, or 1.50, which is an enhancement of 32 percent. The original lineament, which was three pixels wide, is five pixels wide in the filtered version.

The eastern (right-hand) portion of the original profile (Figure 8-16C) has a second lineament marked by a change in values from 40 to 45 along an edge that has no width. The original contrast ratio (45/40 = 1.13) is increased by 27 percent in the enhanced image (50/35 = 1.43). The original edge is expanded to a width of two pixels.

Figure 8-17A is a computer-generated synthetic image with a uniform background (DN = 127). The left portion of the image is crossed by a dark band (DN = 107). The central portion is crossed by a bright band (D = 147). In the right portion of the image, an edge is formed at the contact of background with a brighter surface (DN = 137). These three linear features have subtle expressions in the original image. The linear features of the synthetic image are similar to those in the digital arrays of Figure 8-16A. The Laplacian filter of Figure 8-16A was applied to the synthetic image. After the value of the filter kernel has been calculated and prior to combining it with the original central data pixel, the calculated value may be multiplied by a weighting factor. The factor weight may be less than 1 or

A. Original image.

B. Nondirectional enhancement.
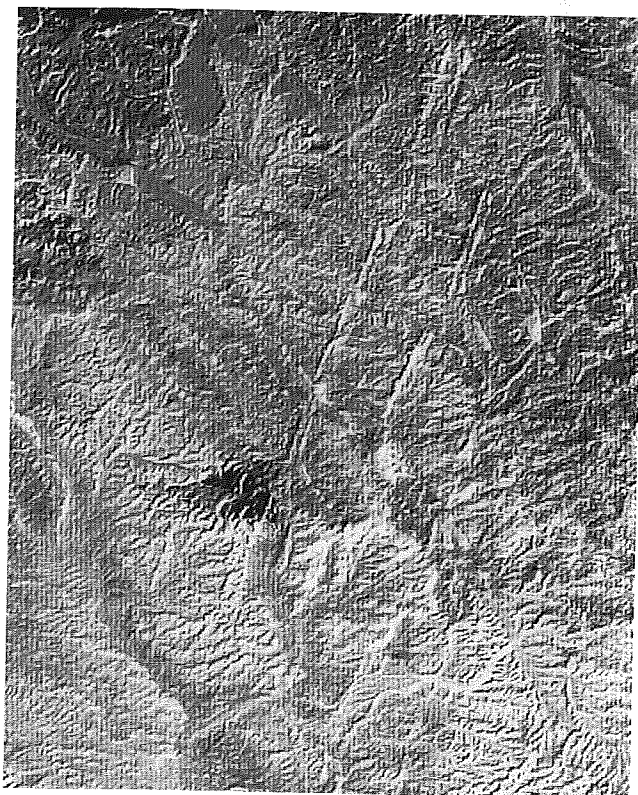
C. Directional enhancement of northeast-trending lineaments.

D. Directional enhancement of northwest-trending lineaments.

Figure 8-18 Edge enhancements of TM images of the Jabal an Naslah area, northwest Saudi Arabia.
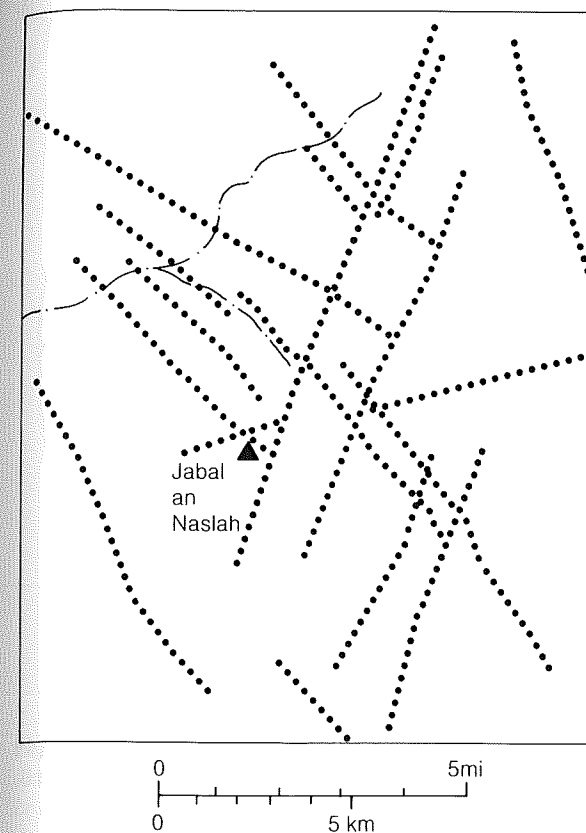
Figure 8-19 Lineaments interpreted from edge-enhanced images of the Jabal an Naslah area (Figure 8-18).

greater than 1 in order to diminish or to accentuate the effect of the filter. The weighted filter value is then combined with the central original pixel to produce the enhanced image.

In Figure 8-17B the calculated kernel value was weighted by a factor of 2.0 to produce the enhanced image. In Figure 8-17C a factor of 5.0 was used. In Figure 8-17D a factor of 10.0 was used, which saturates the brightest values to a DN of 255 and the darkest to a DN of 0. The filtering has significantly enhanced the expression of the original lineaments in Figure 8-17A.

Figure 8-18 shows nondirectional edge enhancement applied to a TM band 4 subscene in northwest Saudi Arabia. The area is a plateau of horizontal strata that is cut by fractures that trend northwest and northeast. Figure 8-19 is a map that shows the major fractures. Figure 8-18B shows the image after processing with the Laplacian filter kernel (Figure 8-16A). Both the northwest and northeast fracture directions are emphasized in the enhanced image.

Many image-processing facilities routinely apply a nondirectional filter to most images, which imparts a "crisper" appearance to the final product.

Directional Filters *Directional filters* are used to enhance linear features that trend in a specific direction, such as N 45°W. Figure 8-20A shows four directional filters that are designed to

enhance the four cardinal directions. Figure 8-20B shows an array of original pixels for terrain with a background DN of 25 that is cut by two lineaments that trend northeast (NE-SW) and northwest (NW-SE). The lineaments have DNs of 30 and are brighter than the background. Figure 8-20C is a profile along line A-B that crosses the lineaments in an east-west direction. The profile shows that each lineament is one pixel wide with a brightness difference from the background of 5 DN.

The filter to enhance NE-SW edges is selected from Figure 8-20A and applied to the original data set. The filter kernel is placed over an array of nine original pixels (three lines by three pixels). Each original pixel is multiplied by the corresponding kernel cell and the results are summed. The resulting kernel value is then combined with the value of the original pixel in the center of the array. Figure 8-20D shows the enhanced pixels that have been processed in this manner. The DNs of the northeast-trending lineament are increased from 30 to 50. In addition, the filter has generated two bands of dark pixels (DN = 15), with a width of one pixel, that trend parallel with the original lineament. Enhanced profile A-B (Figure 8-20E) graphically shows the effects of the directional edge enhancement. Compare this profile with the profile of the original data (Figure 8-20C). The DNs of the original lineament differ from the background by 5 DN for a brightness difference of 20 percent (5/25 = 20%). The three parallel bands of the enhanced lineament differ from the background by a total of 35 DN (25 + 10 = 35) for a brightness difference of 140 percent (35/25 = 140%). The brightness difference is enhanced by 700 percent (140%/20% = 700%). The directional filter also enhances the geometric expression of the lineament. The original lineament is one pixel wide. The enhanced lineament is three pixels wide. Figure 8-20D shows the enhanced lineament (DN = 50) and the two parallel bands (DN = 15). Cross section A-B (Figure 8-20E) crosses the lineament obliquely and therefore gives a misleading impression of the geometric relationships. A cross section (not shown) drawn normal to the lineament (Figure 8-20D) shows that the enhanced lineament is three pixels wide. The geometric expression is enhanced by 300 percent (3 pixel width/1 pixel width = 300%). The key point is that the northeast-trending lineament is strongly enhanced, but the northwest-trending lineament is completely unchanged by this process.

In Figures 8-20F and 8-20G the filter kernel to enhance northwest-trending edges is applied to the original array of pixels. The brightness difference and the geometric expression of the northwest-trending lineament are enhanced in the same manner described above. The northeast-trending lineament is completely unchanged. In summary, the two directional filters have selectively enhanced the northeast- and northwest-trending lineaments by 300 percent in width and 700 percent in brightness difference.

The filters in Figure 8-20A can be modified to enhance linear features trending at directions other than the four cardinal directions, as described by Haralick (1984). Directional edge-enhancement filters were applied to the original Landsat

A. Filters for directional edge enhancement.

	Enhance N-S edge			Enhance E-W edge			Enhance NE-SW edge			Enhance NW-SE edge	
0	0	0	0	-2	0	-2	0	0	0	0	-2
-2	4	-2	0	4	0	0	4	0	0	4	0
0	0	0	0	-2	0	0	0	-2	-2	0	0

B. Original data set.

A● ... B●

25	25	30	25	25	25	25	25	25	25	30	25	25
25	25	25	30	25	25	25	25	25	30	25	25	25
25	25	25	25	30	25	25	25	30	25	25	25	25
25	25	25	25	25	30	25	30	25	25	25	25	25
25	25	25	25	25	25	30	25	25	25	25	25	25
25	25	25	25	25	30	25	30	25	25	25	25	25
25	25	25	25	30	25	25	25	30	25	25	25	25
25	25	25	30	25	25	25	25	25	30	25	25	25
25	25	30	25	25	25	25	25	25	25	30	25	25

C. Profile of original data

Northwest-trending lineament — Northeast-trending lineament

Brightness difference 5 DN

D. Northeast-trending edges enhanced.

25	25	30	25	25	25	15	25	50	25	15
25	25	25	30	25	15	25	50	25	15	25
25	25	25	25	30	25	50	25	15	25	25
25	25	25	15	25	30	25	15	25	25	25
25	25	15	25	50	25	30	25	25	25	25
25	15	25	50	25	15	25	30	25	25	25
15	25	50	25	15	25	25	30	25	25	25
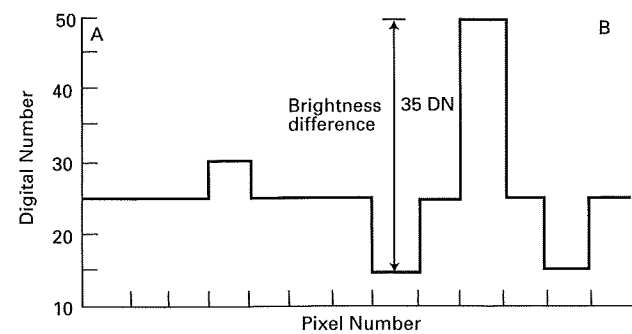
E. Profile A-B of enhanced northeast-trending edges.

Brightness difference 35 DN

F. Northwest-trending edges enhanced.

15	25	50	25	15	25	25	25	30	25	25
25	15	25	50	25	15	25	30	25	25	25
25	25	15	25	50	25	30	25	25	25	25
25	25	25	15	25	30	25	15	25	25	25
25	25	25	30	25	50	25	15	25	25	25
25	25	25	30	25	15	25	50	25	15	25
25	25	30	25	25	25	15	25	50	25	15
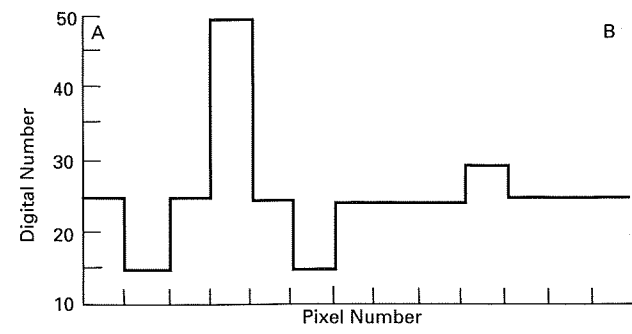
G. Profile A-B of enhanced northwest-trending edges.

Figure 8-20 Edge enhancement using a directional filter.

subscene in Saudi Arabia (Figure 8-18A). In Figure 8-18C, the northeast-trending lineaments are preferentially enhanced. In Figure 8-18D, the northwest-trending lineaments are preferentially enhanced. Comparing Figures 8-18C and 8-18D with the original image (Figure 8-18A) shows that both the brightness difference and the geometric width of the lineaments are selectively enhanced.

Figure 8-18 also compares the effects of directional filters with the effects of nondirectional filters. The nondirectional filter enhances both the northeast-trending lineaments and the northwest-trending lineaments (Figure 8-20B). The directional filters preferentially enhance either the northeast-trending lineaments (Figure 8-20C) or the northwest-trending lineaments (Figure 8-20D). Directional edge enhancement is a valuable technique for selectively improving both the brightness difference and the geometric width of linear features.

Intensity, Hue, and Saturation Transformations

The additive and subtractive systems of primary colors were described in Chapter 2. An alternate approach to color is the *intensity, hue, and saturation (IHS) system,* which is useful because it presents colors more nearly as they are perceived by humans. The IHS system is based on the color sphere (Figure 8-21) in which the vertical axis represents intensity, the radius represents saturation, and the circumference represents hue. The *intensity* (I) axis represents brightness variations and ranges from black (0) to white (255); no color is associated with this axis. *Hue* (H) represents the dominant wavelength of color. Hue values commence with 0 at the midpoint of red tones and increase counterclockwise around the circumference of the sphere to conclude with 255 adjacent to 0. *Saturation* (S) represents the purity of color and is represented by the radius that ranges from 0 at the center of the color sphere to 255 at the circumference. A saturation of 0 represents a completely impure color in which all wavelengths are equally represented as a shade of gray. Intermediate values of saturation are pastel shades, whereas high values are purer and more intense colors. Buchanan (1979) describes the IHS system in detail.

Figure 8-21 Coordinate system for the intensity, hue, and saturation (IHS) transformation. The color at point A has the following values: $I = 205$, $H = 75$, $S = 130$ (undersaturated).

Thermopolis, Wyoming, Example When any three spectral bands of TM (or other multispectral data) are combined in the BGR system, the resulting color images typically lack saturation, even though the bands have been contrast-stretched. Plate 11A is a normal color image prepared from TM bands 1, 2, and 3 of the Thermopolis, Wyoming, subscene. The individual 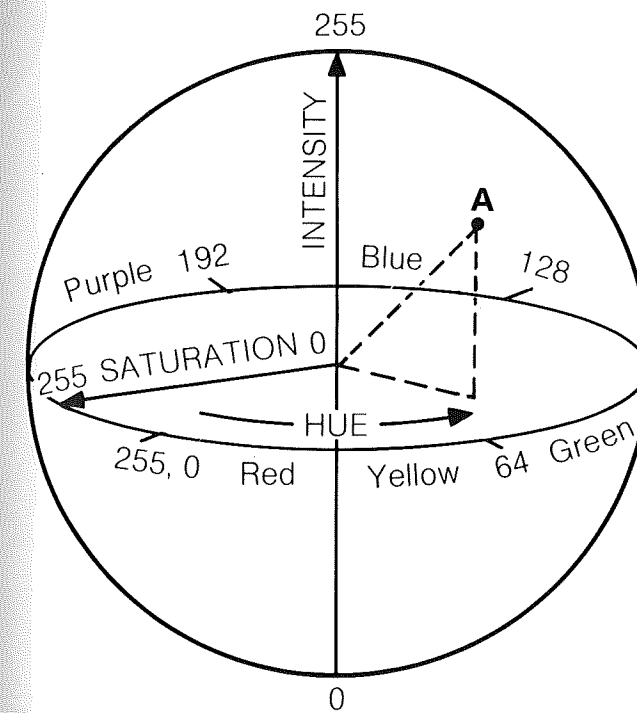bands were contrast-enhanced, but the color image has the pastel appearance that is typical of many Landsat images. The undersaturation is due to the high degree of correlation between spectral bands. High reflectance values in the green band, for example, are accompanied by high values in the blue and red bands, so pure colors are not produced. To correct this problem, a method of enhancing saturation was developed that consists of the following steps:

1. Transform the three bands of data from the BGR system into the IHS system in which the three component images represent intensity, hue, and saturation. This IHS transformation was applied to TM bands 1, 2, and 3 of the Thermopolis subscene to produce the intensity, hue, and saturation images illustrated in Figure 8-22. The intensity image (Figure 8-22A) is dominated by albedo and topography. Sunlit slopes have high intensity values (bright tones), and shadowed areas have low values (dark tones). The airport runway and water in the Wind River have low values (see Figure 3-7H for locations). Vegetation has intermediate intensity values, as do most of the rocks. In the hue image (Figure 8-22B) red beds of the Chugwater Formation have conspicuous dark tones caused by low values assigned to red hues. Vegetation has intermediate to light-gray values assigned to the green hue. The original saturation image (Figure 8-22C) is very dark because of the lack of saturation in the original TM data. Only the shadows and river are bright, indicating high saturation for these features.
2. Apply a linear contrast stretch to enhance the original saturation image (Figure 8-22D). Note the overall increased brightness of the enhanced image. Also note the improved discrimination between terrain types.
3. Transform the intensity, hue, and enhanced saturation image from the IHS system back into the three images of the BGR system. These enhanced BGR images were used to prepare the new color composite image of Plate 11B, which is a significant improvement over the original version in Plate 11A. In the IHS version, note the wide range of colors and improved discrimination between colors. Some bright green fields are distinguishable in vegetated areas that were obscure in the original. The wider range of color tones helps separate rock units.

Figure 8-23 shows graphically the relationship between the BGR and IHS systems. Numerical values may be extracted from this diagram for expressing either system in terms of the other. In Figure 8-23 the circle represents a horizontal section through the equatorial plane of the IHS sphere, with the intensity axis passing vertically through the plane of the diagram.
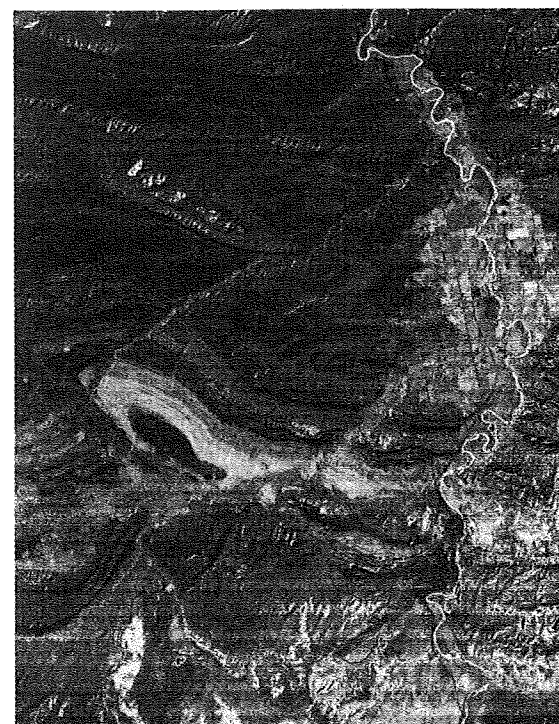
A. Intensity image.

B. Hue image.

C. Saturation image, original.

D. Saturation image, stretched.

Figure 8-22 Images created by the IHS transformation of TM bands 1, 2, and 3 of the Thermopolis, Wyoming, subscene.
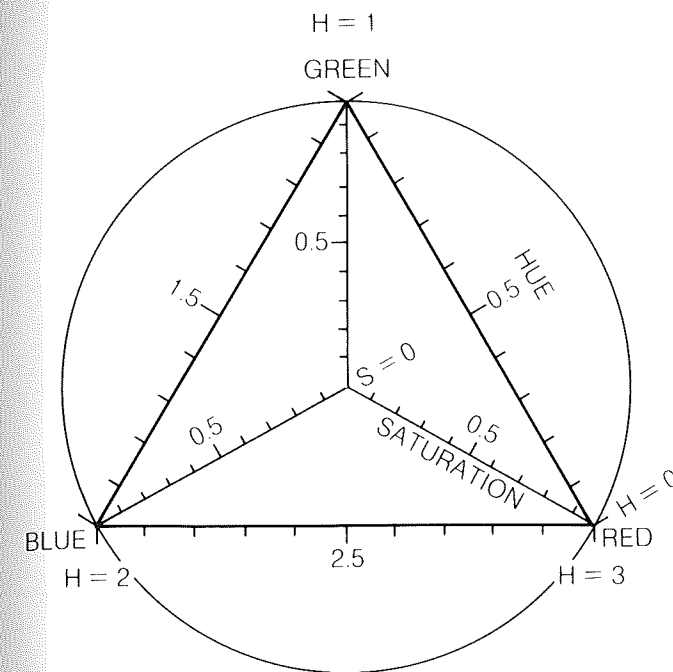

Figure 8-23 Diagram showing the relationship between the BGR and IHS systems.

The corners of the equilateral triangle are located at the positions of the red, green, and blue hues. Hue changes in a counterclockwise direction around the triangle, from red (0), to green (1), to blue (2), and again to red (3). Values of saturation are 0 at the center of the triangle and increase to a maximum of 1 at the corners. Any perceived color is described by a unique set of IHS values; in the BGR system, however, different combinations of additive primaries can produce the same color. The IHS values can be derived from BGR values through the transformation equations

$$I = R + G + B \tag{8-1}$$

$$H = I - 3B \tag{8-2}$$

$$S = I \tag{8-3}$$

for the interval $0 < H < 1$, extended to $1 < H < 3$. After enhancing the saturation image, the IHS values are converted back into BGR images by inverse equations.

Western Bolivia Example Saturation enhancement is also effective in other regions and other combinations of spectral bands. Plate 11C is a TM 2-4-7 image in western Bolivia. The eastern portion consists of volcanic features of the Andes and the western portion is alluvial deposits. The bands were contrast-enhanced but are dominated by monotonous undersaturated hues of brown, tan, and gray. Plate 11D is the same image after saturation enhancement. Subtle color differences are emphasized, and much more geologic information was interpreted from the enhanced image.

The IHS transform has other applications in addition to enhancing the saturation of images. The traditional method of enhancing edges on multispectral images, such as TM, is to enhance each of the three bands separately. It is more efficient to transform the three TM bands into IHS components, and then to apply edge enhancement to the intensity component. When the image is transformed back into BGR components, the edge enhancement is applied to each of the bands. This operation may be combined with the saturation enhancement.

The IHS transformation is also used to produce combination images, as described in the following section.

Combination Images

Different images that have been digitally merged are called *combination images*. For example, Landsat TM color images display three spectral bands but have a relatively coarse spatial resolution (30 m). SPOT pan images have good resolution (10 m) but display only a single spectral band. A combination image can display the spectral characteristics of the TM with the spatial resolution of SPOT. Plate 12A is a TM IR color image (bands 2, 3, and 4 shown as blue, green, and red) of the northern portion of Los Angeles. Figure 8-24 is a SPOT pan image and a map of the same area. Comparing the two images shows the advantages of each version and the reason for combining them. Spatial details of buildings and street patterns are clearly visible in the SPOT image but are not recognizable in the TM image. The circular streets in the large parking lot that surrounds Dodger Stadium are clearly seen in the SPOT but not in the TM. The sparse vegetation, however, has a distinctive red signature in the TM image but is not recognizable in the SPOT image. Various shades of blue in the TM indicate spectral signatures of different categories of land use. These spectral characteristics are absent in SPOT, which does, however, show details of size, shape, and spacing (density) of buildings and streets. The two images clearly complement each other; a combination of the two would be valuable for the interpreter.

The IHS transformation is used to combine such images in the following manner:

1. For the TM image, resample each original pixel (30 by 30 m) into nine pixels (10 by 10 m) to match the SPOT size.
2. Use ground control points to register the TM image to the SPOT image.
3. Transform the resampled TM color image into its IHS components.
4. Discard the TM intensity component and replace it with the SPOT data.
5. Transform the new set of IHS components back into BGR components.

Plate 12B is the combined TM/SPOT image with 10-m ground resolution cells and three spectral bands.

A. SPOT pan image (10-m resolution).
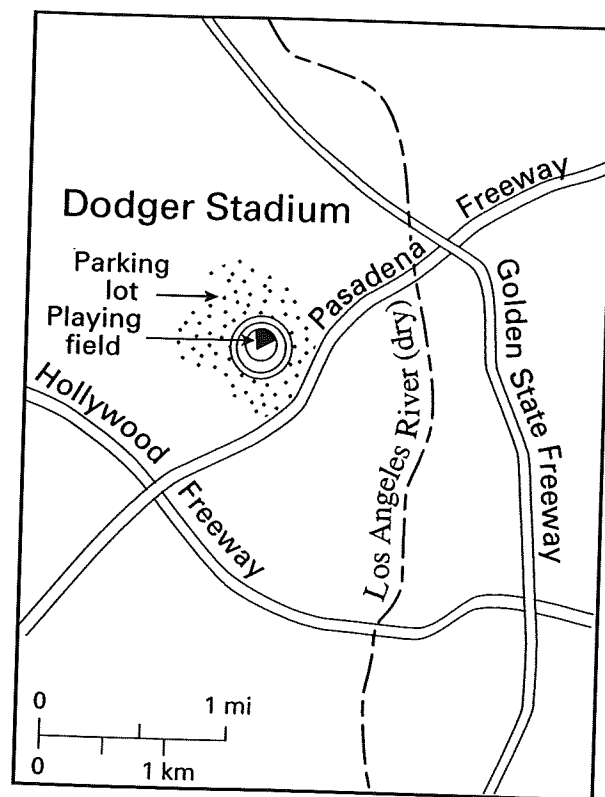
B. Location map.

Figure 8-24 SPOT panchromatic image and map, Los Angeles, California.

A. Topographic map. Contour interval = 200 ft.

B. Location map showing anticlines and outcrops of the Chugwater Formation.

Figure 8-25 Maps of Sheep Mountain, Wyoming.

This technique is used to combine other images, such as radar and TM images. The combination image merges the shadows and highlights plus high spatial resolution of radar with the spectral information from TM. It is more efficient to interpret the combination image than to interpret TM and radar images separately and combine the results. Chavez, Sides, and Anderson (1991) compare three methods of merging images, including the IHS technique.

Digital Mosaics

Mosaics of Landsat images may be prepared by manually matching and splicing together individual images, as shown for the Central Arabian Arch in Plate 4. Differences in contrast and tone between adjacent images may cause the checkerboard pattern that is common on many mosaics. This problem is minimized by preparing mosaics directly from the digital CCTs.

Plate 13 is a digital mosaic of six TM images of southern California prepared by R. E. Crippen of the Jet Propulsion Laboratory (JPL). Earthquake data and traces of faults are added to the mosaic and are discussed in Chapter 13. The six images were acquired at different dates and seasons, which causes major color differences between adjacent scenes. For the area of sidelap between adjacent images, the computer op-erator compared histograms for corresponding bands of each image and adjusted the histograms to match. This procedure was successful, as shown by the excellent match of colors throughout the mosaic. Adjacent images were then geometrically registered to each other by identifying common ground control points (GCPs) in the regions of sidelap. Pixels were then geometrically adjusted to match the desired map projection. The next step was to eliminate from the digital file the duplicate pixels within the areas of overlap. Optimum contrast stretching was then applied to all the pixels, producing a uniform appearance throughout the mosaic.

Synthetic Stereo Pairs

The stereo pairs of aerial photographs (see Chapter 2) and SPOT images (see Chapter 4) demonstrate the value of stereo images with vertical exaggeration. Landsat images, however, have no stereo capability, aside from negligible sidelap. *Synthetic stereo pairs* are stereo models produced by merging a single image with digital topographic data. Digital topographic data 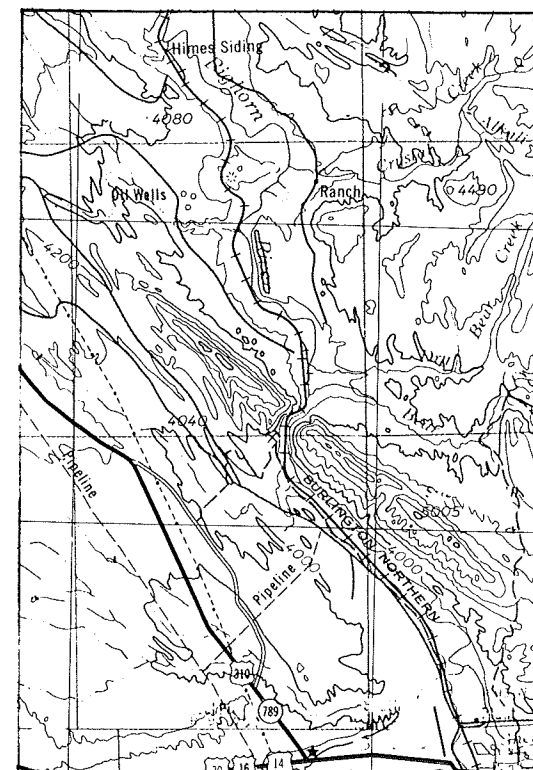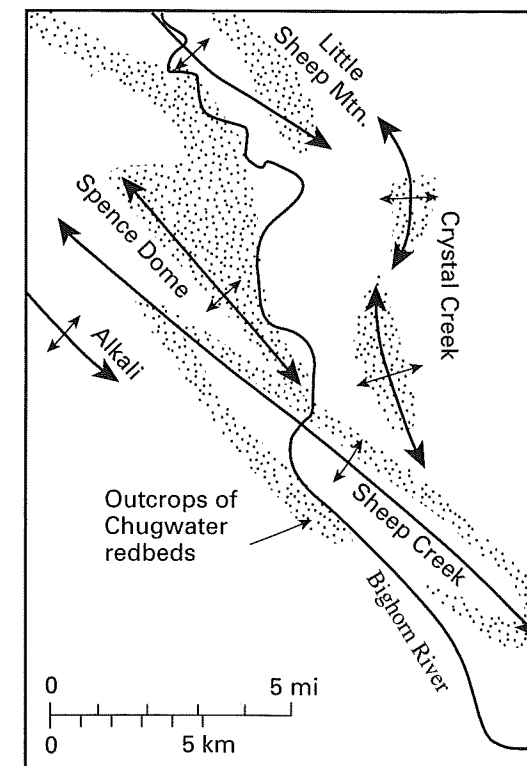are produced by digitizing topographic contour maps, such as Figure 8-25A, into raster arrays of pixels. Each pixel represents a ground resolution cell and records the average elevation of the cell. Digital topographic data are also available from the Topographic Division of the U.S. Geological Survey. Synthetic stereo pairs are produced for a TM image by the following procedure:

1. The digital topographic data are resampled into pixels that match the pixel size (30 by 30 m) of the TM image.
2. Ground control points are used to register Landsat pixels with topographic pixels. Each TM pixel now has an elevation value in addition to its spectral band values.
3. The operator selects a center point on the image (that will be analogous to the principal point of an aerial photograph) and designates the amount of vertical exaggeration for the stereo pair.
4. The computer program then radially displaces the pixels from the principal point to produce a new image with paral-lax, such as that shown for the aerial photographs in Chapter 2. The computer then shifts to a conjugate principal point in the image and generates the second image for the synthetic stereo pair.

Plate 12C is a synthetic stereo pair that was produced in this manner from a single TM 2-3-4 IR color image. View the images with a stereoscope to appreciate the three-dimensional effect and vertical exaggeration. Figure 8-25A is a topographic map of the area, which is located in the northeast portion of the Bighorn Basin, Wyoming. Sedimentary strata are folded into an array of anticlines that are identified in the location map (Figure 8-25B). The major topographic and geologic feature is the northwest-trending Sheep Mountain anticline with a ridge of light-colored late Paleozoic strata exposed in the core. The core is surrounded by red beds of the Chugwater Formation (Triassic), which have a distinctive yellow signature in the image, and is indicated by the stippled pattern in Figure 8-25B. Sandstones and shales of Mesozoic age form ridges and valleys with gray and blue signatures. The fold axes and attitudes (dip and strike) of the strata are readily interpreted from the stereo pair.

Digital Perspective Images

Digital perspective images are three-dimensional views produced from digital topographic data that have been merged with other data sets. Plate 14A is a perspective image of the north flank of the San Bernardino Mountains and the Antelope Valley in southern California. R. E. Crippen of the JPL produced the image in the following manner:

1. A SPOT pan image was selected as the "master" image. Digital topographic data and a TM 2-4-7 image were resampled to 10-by-10-m pixels and registered with the SPOT data, using GCPs.

2. The merged data were geometrically transformed into a three-dimensional view of the terrain. The operator specified the look direction (toward the west) and vertical exaggeration.

The combination of topography and spectral information on the perspective image emphasizes differences between the rugged, vegetated mountains and the low-lying barren desert of the Antelope Valley. The two terrains are separated by a series of faults that strike parallel with the mountain front. The topographic scarps that mark the faults are accentuated by the perspective view and vertical exaggeration. Of special interest is the Blackhawk landslide, which forms a dark lobe in the lower right portion of the image. This massive prehistoric slide originated on the north flank of the mountains and moved far out into the desert. Details of the landslide are given in Chapter 13.

INFORMATION EXTRACTION

Image restoration and enhancement processes utilize computers to provide corrected and improved images for study by human interpreters. The computer makes no decisions in these procedures. However, the processes that comprise information extraction do utilize the computer's decision-making capability to identify and extract specific pieces of information. A human operator must instruct the computer and must evaluate the significance of the extracted information.

Principal-Component Images

If we compare individual TM bands such as the Thermopolis subscene (Chapter 3), we note a strong similarity. Areas that are bright or dark in one band tend to be bright or dark in the other bands. This relationship is shown diagrammatically in Figure 8-26, in which DNs for TM band 1 are plotted versus TM band 2. Data points are distributed in an elongate band, which shows that as DNs increase for one band, they increase for the other band. If for any pixel we know the DN for band 1, we can predict the approximate value in band 2. The data are said to be strongly correlated. This correlation means that there is much redundancy of information in a multispectral data set. If this redundancy were reduced, the amount of data required to describe a multispectral image could be compressed.

The *principal-components transformation*, originally known as the Karhunen-Loéve transformation (Loéve, 1955), is used to compress multispectral data sets by calculating a new coordinate system. For the two bands of data in Figure 8-26, the transformation defines a new axis (y_1) oriented in the long dimension of the distribution and a second axis (y_2) perpendicular to y_1. The mathematical operation makes a linear combination of pixel values in the original coordinate system that results in pixel values in the new coordinate system:
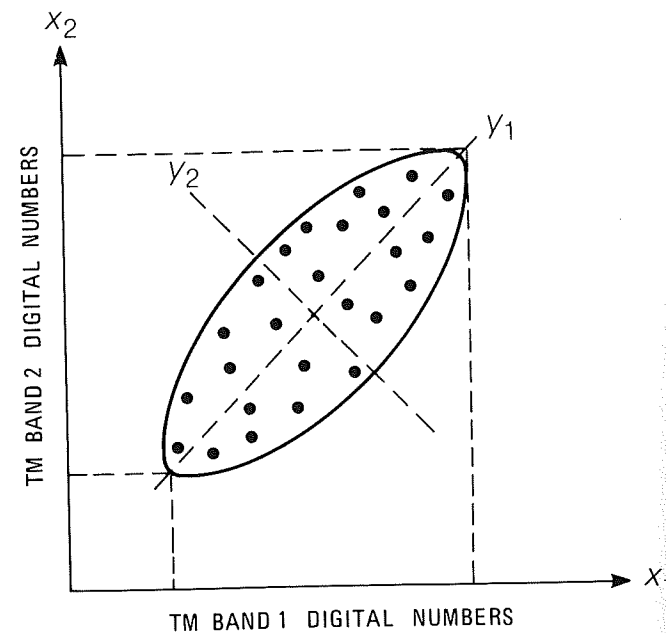

Figure 8-26 Plot of DNs for TM band 1 (axis x_1) and band 2 (axis x_2) showing correlation between these bands. The principal-components transformation was used to generate a new coordinate system (y_1, y_2). After Swain and Davis (1978, Figure 7.9).

$$y_1 = a_{11} x_1 + a_{12} x_2 \qquad (8\text{-}4)$$

$$y_2 = a_{21} x_1 + a_{22} x_2 \qquad (8\text{-}5)$$

where

(x_1, x_2) = pixel coordinates in the original system

(y_1, y_2) = coordinates in the new system

a_{11}, a_{12}, a_{22} = constants

In Figure 8-26 note that the range of pixel values for y_1 is greater than the ranges for either of the original coordinates, x_1 or x_2, and that the range of values for y_2 is relatively small.

The same principal-components transformation may be carried out for multispectral data sets consisting of any number of bands. Additional coordinate directions are defined sequentially. Each new coordinate is oriented perpendicular to all the previously defined directions and in the direction of the remaining maximum density of pixel data points. For each pixel, new DNs are determined relative to each of the new coordinate axes. A set of DN values is determined for each pixel relative to the first principal component. These DNs are then used to generate an image of the first principal component. The same procedure is used to produce images for the remaining principal components. The preceding description of the principal-components transformation is summarized from Swain and Davis (1978); additional information is given in Moik (1980).

A principal-components transformation was performed on the three visible and three reflected IR bands of TM data for the Thermopolis, Wyoming, subscene. Each pixel was assigned six new DNs corresponding to the first through the sixth principal-component coordinate axes. Figure 8-27 illustrates the six principal-component (PC) images, which have been contrast-enhanced. As noted earlier, each successive principal component accounts for a progressively smaller proportion of the variation of the original multispectral data set. These percentages of variation are indicated for each PC image in Figure 8-27 and are plotted graphically in Figure 8-28. The first three PC images contain 97 percent of the variation of the original six TM bands, which is a significant compression of data. PC image 1 (Figure 8-27A) is dominated by topography, expressed as highlights and shadows, that is highly correlated in all six of the original TM bands. PC image 2 (Figure 8-27B) is dominated by differences in albedo that also correlate from band to band because pixels that are bright in one TM band tend to be bright in adjacent bands. The least-correlated data are noise such as line striping and dropouts, which occur in different detectors and different bands. In Figure 8-27, noise dominates PC images 4, 5, and 6, which together account for only 2.6 percent of the original variation. Note, however, that PC image 6 (Figure 8-27F) displays parallel arcuate dark bands in the outcrop belt of the Chugwater Formation that may represent lithologic variations in this unit.

Any three PC images can be combined in red, green, and blue to create a color image. Plate 14B was produced by combining PC images from Figure 8-27 in the following fashion: PC 2 = red, PC 3 = green, PC 4 = blue. PC image 1 was not used in order to minimize topographic effects. As a result, the color PC image displays a great deal of spectral variation in the vegetation and rocks, although the three images constitute only 10.7 percent of the variation of the original data set.

Examination of the original TM bands for the Thermopolis subscene in Chapter 3 shows that the visible bands 1, 2, and 3 are highly correlated with each other, as are the three reflected IR bands 4, 5, and 7. Rather than transform all six bands into six PC images, it is useful to transform bands 1, 2, and 3 into three PC images and bands 4, 5, and 7 into three PC images.

In summary, the principal-components transformation has several advantages:

1. Most of the variance in a multispectral data set is compressed into the first two PC images.
2. Noise is generally relegated to the less-correlated PC images.
3. Spectral differences between materials may be more apparent in PC images than in individual bands.

Ratio Images

Ratio images are prepared by dividing the DN value in one band by the corresponding DN value in another band for each pixel. The resulting values are plotted as a ratio image. Figure 8-29 illustrates some ratio images prepared from TM bands of the Thermopolis subscene. In a ratio image the black and white extremes of the gray scale represent pixels having the greatest difference in reflectivity between the two spectral bands. The darkest signatures are areas where the denominator of the ratio is greater than the numerator. Conversely, the numerator is greater than the denominator for the brightest signatures. Where denominator and numerator are the same, there is no difference between the two bands.

For example, the spectral reflectance curve for vegetation (Figure 3-1) shows a maximum reflectance in TM band 4 (reflected IR) and a lower reflectance in band 2 (green). Figure 8-29C is the ratio image 4/2, which is produced by dividing DNs for band 4 by the DNs for band 2. The brightest signatures in this image correlate with the cultivated fields along the Wind River and Owl Creek (Figure 3-7H). Figure 8-29A is the ratio image 3/1 (red/blue), in which red beds of the Chugwater outcrops have very bright signatures.

Any three ratio images may be combined in red, green, and blue to produce a color image. In Plate 14C the ratio images 3/1, 5/7, and 3/5 are combined as red, green, and blue, respectively. Compare this image with the various Thermopolis color images (Plate 2) and the interpretation map (Figure 3-8). The signatures of the ratio color image express more geologic information and have greater contrast between units than do color images of individual TM bands. An advantage of ratio images is that they extract and emphasize differences in spectral reflectance of materials. A disadvantage of ratio images is that they suppress differences in albedo; materials that have different albedos but similar spectral properties may be indistinguishable in ratio images. Another disadvantage is that any noise is emphasized in ratio images.

Ratio images also minimize differences in illumination conditions, thus suppressing the expression of topography. In Figure 8-30 a red siltstone bed crops out on both the sunlit and shadowed sides of a ridge. In the individual Landsat TM bands 1 and 3, the DNs of the siltstone are lower in the shadowed area than in the sunlit outcrop, which makes it difficult to follow the siltstone bed around the hill. Values of the ratio image 3/1, however, are identical in the shadowed and sunlit areas, as shown by the chart in Figure 8-30; thus the siltstone has similar signatures throughout the ratio image. Highlights and shadows are notably lacking in the ratio images of Figure 8-29.

In addition to ratios of individual bands, a number of other ratios may be computed. An individual band may be divided by the average for all the bands, resulting in a normalized ratio image. Another ratio combination is produced by dividing the difference between two bands by their sum; for example, (band 4 − band 5)/(band 4 + band 5). Ratios of this type are used to process AVHRR data, as described in Chapter 9.

Multispectral Classification

For each pixel in a Landsat TM image, the spectral brightness is recorded for six spectral bands in the visible and reflected IR
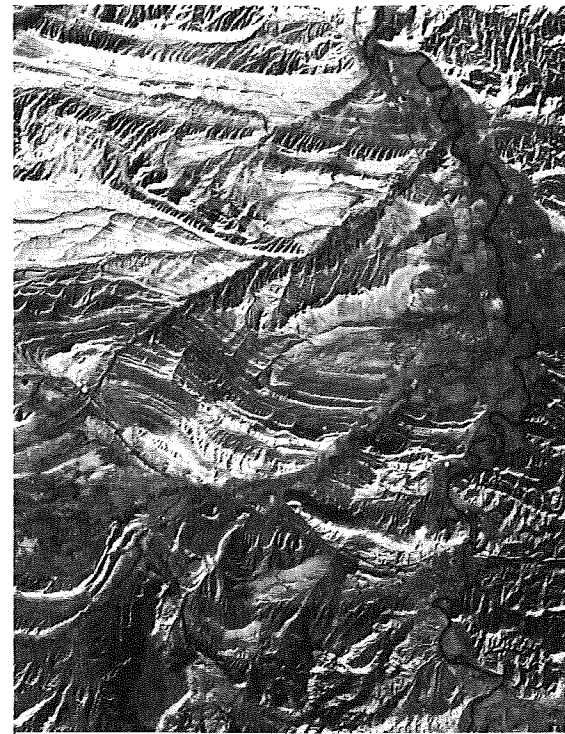
A. PC image 1 (88.4 percent).

B. PC image 2 (6.6 percent).

E. PC image 5 (0.5 percent).

F. PC image 6 (0.3 percent).

Figure 8-27 (*continued*)

C. PC image 3 (2.4 percent).

D. PC image 4 (1.8 percent).

Figure 8-27 Principal-component (PC) images of the Thermopolis, Wyoming, subscene. PC images were generated from the six visible and reflected IR bands of TM images. The percentage of variance represented by each PC image is shown.

regions. A pixel may be characterized by its *spectral signature*, which is determined by the relative reflectance in the different wavelength bands. *Multispectral classification* is an information-extraction process that analyzes these spectral signatures and then assigns pixels to classes based on similar signatures.

Procedure Multispectral classification is illustrated diagrammatically with a Landsat image (Figure 8-31A) of southern California that covers the Salton Sea, the Imperial Valley, and adjacent mountains and deserts. Figure 8-32A shows reflectance spectra for water, agriculture, desert, and mountains that are derived from TM bands. The data points are plotted at the center of each TM bandpass. In Figure 8-32B the reflectance ranges of bands 2, 3, and 4 form the axes of a three-dimensional coordinate system. The solid dots are the loci of the four terrain categories in Figure 8-32A. Plotting additional pixels of the different terrain types produces three-dimensional clusters or ellipsoids. The surface of an ellipsoid forms a *decision boundary*, which encloses all pixels for that terrain category. The volume inside the decision boundary is called the *decision space*. Classification programs differ in their criteria for defining decision boundaries. In many programs the analyst is able to modify the boundaries to achieve optimum results. For the sake of simplicity the cluster diagram (Figure 8-32B) is shown with only three axes. In actual practice the computer employs a separate axis for the six TM bands.
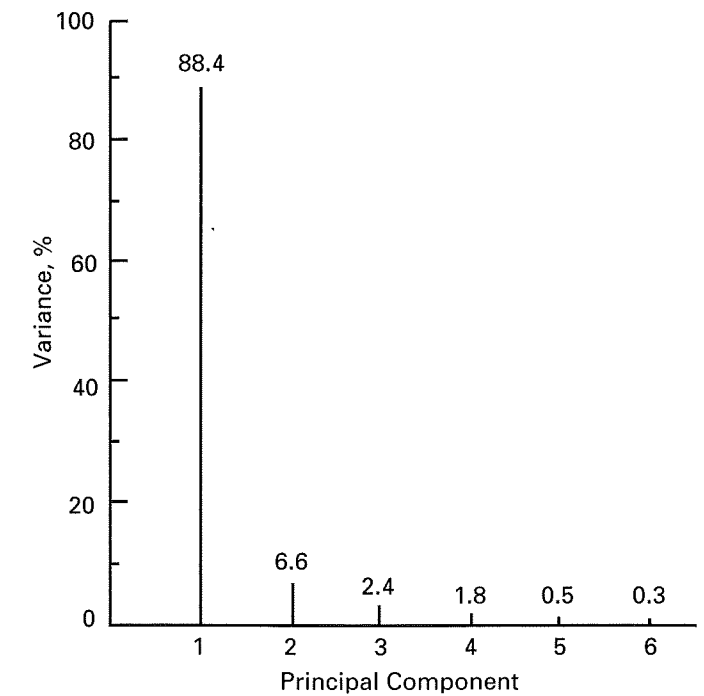
Figure 8-28 Plot showing the percentage of variance represented by PC images of the Thermopolis, Wyoming, subscene (Figure 8-27).
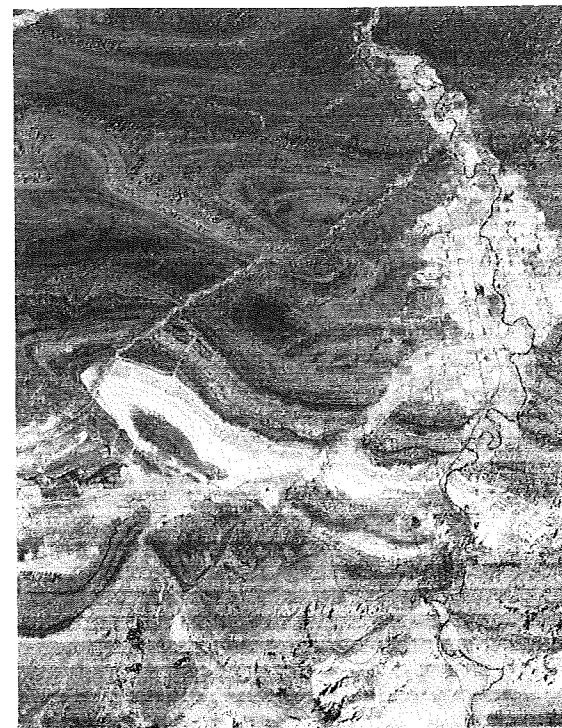
A. Ratio image 3/1.

B. Ratio image 3/5.
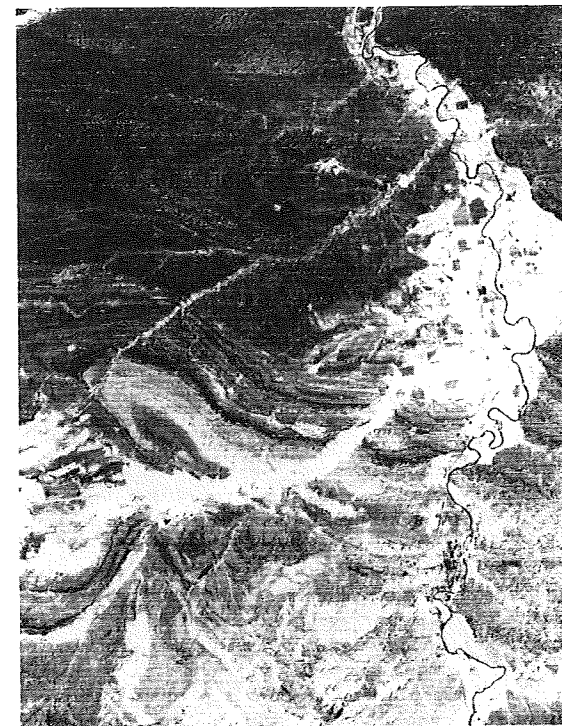
C. Ratio image 4/2.
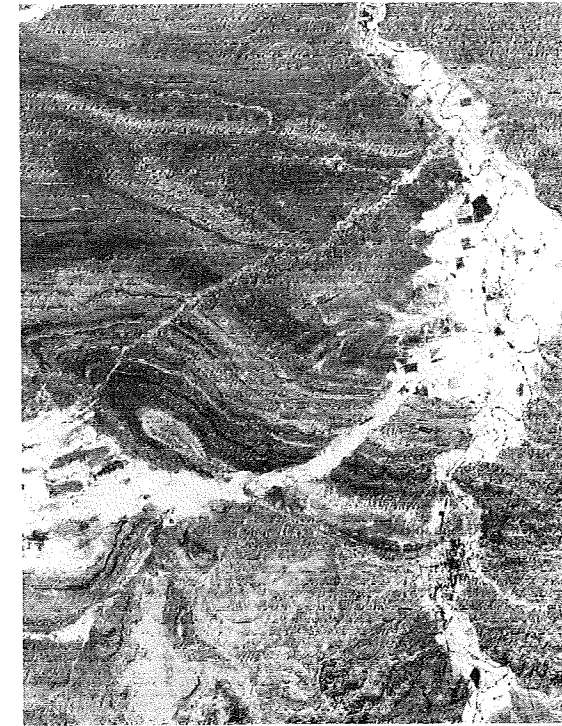
D. Ratio image 5/7.

Figure 8-29 Ratio images of Landsat TM bands of the Thermopolis, Wyoming, subscene. The images have been contrast-enhanced.
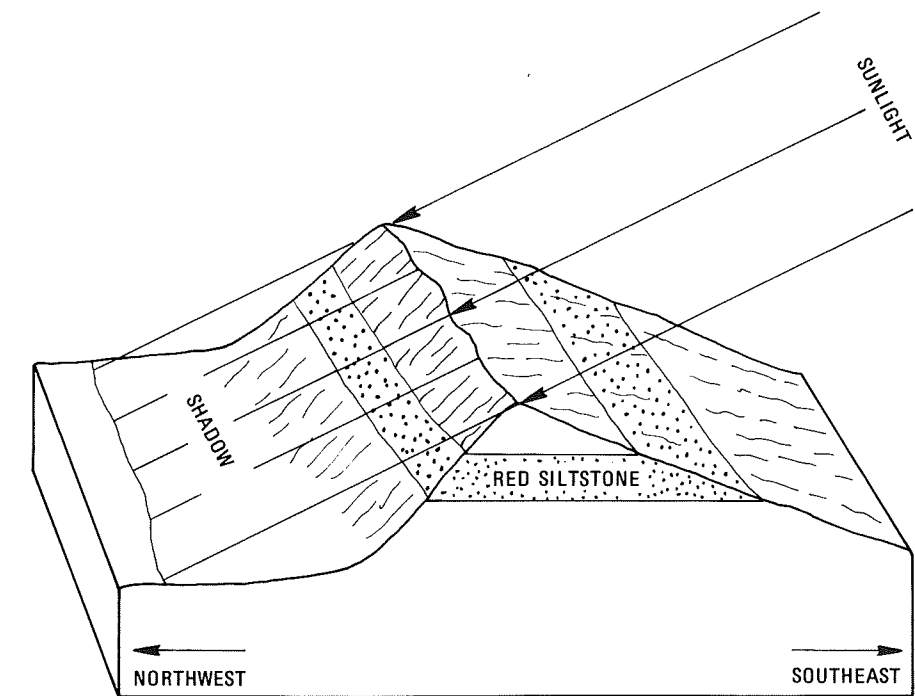
SILTSTONE REFLECTANCE

ILLUMINATION	TM BAND 3	TM BAND 1	RATIO 3/1
Sunlight	94	42	2.24
Shadow	76	34	2.23

Figure 8-30 Suppression of illumination differences on a ratio image.

Once the boundaries for each cluster, or *spectral class*, are defined, the computer retrieves the spectral value for each pixel and determines its position in the classification space. Should the pixel fall within one of the clusters, it is classified accordingly. Pixels that do not fall within a cluster are considered unclassified. In practice the computer calculates the mathematical probability that a pixel belongs to a class; if the probability exceeds a designated threshold (represented spatially by the decision boundary), the pixel is assigned to that class. Applying this method to the digital data of the Salton Sea and the Imperial Valley scene produces the classification map of Figure 8-31B. The blank areas (unclassified category) occur at the boundaries between classes where the pixels include more than one terrain type.

There are two major approaches to multispectral classification:

1. **Supervised classification** The analyst defines on the image a small area, called a *training site*, which is representative of each terrain category, or class. Spectral values for each pixel in a training site are used to define the decision space for that class. After the clusters for each training site are defined, the computer then classifies all the remaining pixels in the scene.

2. **Unsupervised classification** The computer separates the pixels into classes with no direction from the analyst.

The two classification methods are compared by applying them to the TM data for the Thermopolis, Wyoming, subscene.

Supervised Classification The first step in the supervised classification is to select training sites for each of the terrain categories. In Figure 8-33 the training sites are indicated by black rectangles. Some categories are represented by more than one training site in order to cover the full range of reflectance characteristics. Figure 8-34 shows TM reflectance spectra for the terrain categories. Note the wider range of

A. Landsat image.

0		20 mi
0		20 km

B. Classification map. A = agriculture, D = desert, M = mountains, W = water, blank = unclassified.

Figure 8-31 Multispectral classification of Landsat data for the Salton Sea and the Imperial Valley, California.

A. Spectral reflectance curves derived from TM bands. The high values in band 1 are caused by selective atmospheric scattering.

B. Three-dimensional cluster diagram for classification.

Figure 8-32 Landsat data used to classify image of the Salton Sea and the Imperial Valley, California.

spectral variation in the reflected IR bands (4, 5, and 7) than in the visible bands (1, 2, and 3). In the first attempt at supervised classification, training sites were selected for each of the geologic formations, but the results showed that individual formations of the same rock type had similar or overlapping spectral characteristics and were assigned to the same class. For example, many of the formations are sandstones, which proved to be spectrally similar despite their different geologic ages. The fi-

nal classification identified rocks as sandstone, shale, and red beds. The resulting supervised classification image (Plate 15A) uses colors to represent the six major terrain classes; black indicates unclassified pixels. The legend identifies each terrain class and the percentage of the map occupied by each class. The classification map may be evaluated by comparing it with Figure 8-33, which is based on geologic maps of the Thermopolis area. Plate 15A shows the major terrain categories accurately. Some narrow belts of the shale class are shown interbedded with the sandstone class; this is correct because several sandstone units, such as the Frontier Formation, include shale beds. The proportion of shale in the classification map is probably understated for the following reason. Shale weathers to very fine particles that are easily removed by wind and water. Sandstone, however, weathers to relatively coarse fragments of sand and gravel that may be transported downslope to partially conceal underlying shale beds. This relationship is shown where the course of dry streams that cross the outcrop of the Cody Shale is classified as sandstone because of the transported sand and sandstone gravel in the streambeds.

Unsupervised Classification Plate 15B shows an unsupervised-classification image, which was produced by a program that automatically defined 16 classes. After the 16 unsupervised classes were calculated, I reviewed them and combined them into the eight classes shown in Plate 15B. Patterns of the sandstone and shale classes are similar to those in the supervised map. The computer recognized two spectral subdivisions of the Chugwater Formation: a lower member shown in red and an upper member shown in orange (Plate 15B, Legend). The lower member is confined to the Chugwater outcrop belt, but the upper member is recognized beyond the Chugwater outcrops, where it also represents patches of reddish soil. The unsupervised classification recognized native vegetation and three distinct classes of agriculture.

Neither classification map recognized the outcrops of carbonate rocks shown in the map of Figure 8-33. The carbonate outcrops are classified as sandstone in both maps. Figure 3-1 shows reflectance spectra for sandstone and limestone, plus the spectral ranges of the TM bands. This figure demonstrates that the broad bandwidths recorded by TM bands lack the spectral resolution to distinguish sandstone from limestone. The supervised and unsupervised classifications failed to separate these rocks because the TM data were inadequate, not because the digital classification methods were inadequate. This example demonstrates the need for multispectral images with finer spectral resolution (narrower bandwidths), such as the images acquired by hyperspectral scanners.

Change-Detection Images

Change-detection images provide information about seasonal or other changes. The information is extracted by comparing two or more images of an area that were acquired at different
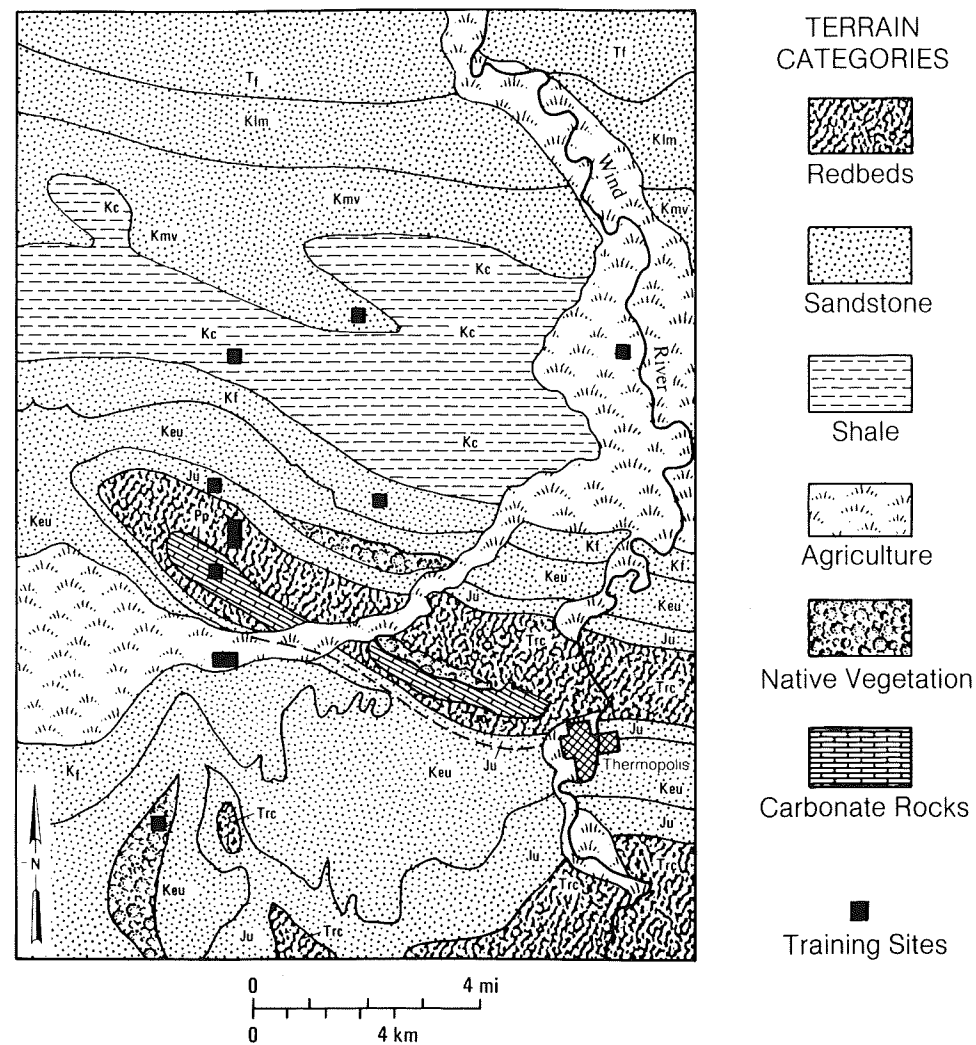
Figure 8-33 Terrain categories and training sites for supervised classification of the Thermopolis, Wyoming, subscene. Abbreviations for formations are given in Figure 3-8.
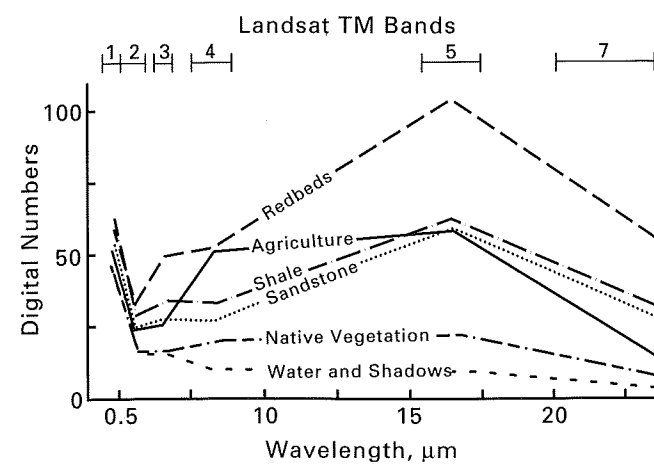

Figure 8-34 Reflectance spectra (from TM bands) of terrain categories shown in Figure 8-33

times. The first step is to register the images using corresponding GCPs. Following registration, the digital numbers of one image are subtracted from those of an image acquired earlier or later. The resulting values for each pixel are positive, negative, or zero; the latter indicates no change. The next step is to plot these values as an image in which a neutral gray tone represents zero. Black and white tones represent the maximum negative and positive differences, respectively. Contrast stretching is employed to emphasize the differences.

The change-detection process is illustrated with Landsat MSS band 5 images of the Goose Lake area of Saskatchewan, Canada (Figure 8-35). The DN of each pixel in the June 27, 1973, image (Figure 8-35B) is subtracted from the DN of the corresponding registered pixel in the September 7, 1973, image (Figure 8-35A). The resulting values are linearly stretched and displayed as the change-detection, or difference, image (Figure 8-35C). The location map aids in understanding
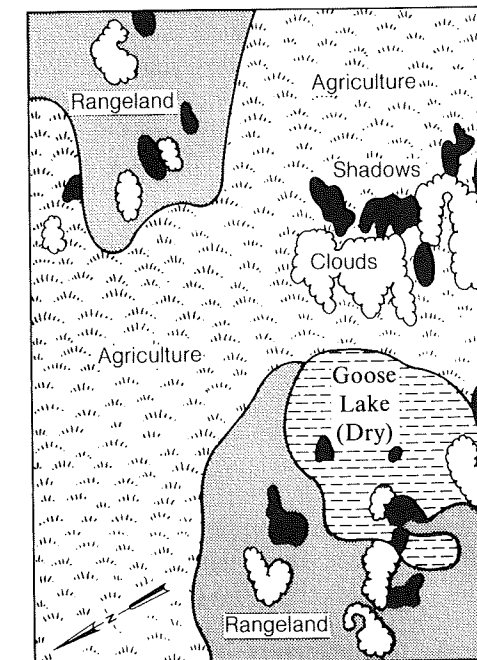

A. September 7, 1973, image.
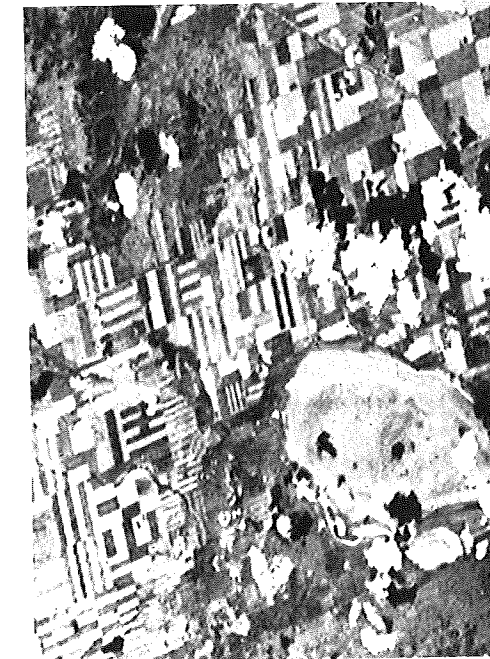
B. June 27, 1973, image.

C. Difference image (image A minus image B).

D. Terrain map.

Figure 8-35 Change-detection image computed from seasonal Landsat MSS images, Saskatchewan, Canada. From Rifman and others (1975, Figures 2-14, 2-15, 2-17).

signatures in the difference image. Neutral gray tones representing areas of little change are concentrated in the northwest and southeast and correspond to forest terrain. Forest terrain has a similar dark signature on both original images. Some patches within the ephemeral Goose Dry Lake have similar light signatures on images A and B, resulting in a neutral gray tone on the difference image. The clouds and shadows that are present only on image B produce dark and light tones, respectively, on the difference image. The agricultural practice of seasonally alternating between cultivated and fallow fields is clearly shown by the light and dark tones on the difference image. On the original images, the fields with light tones have crops or stubble and the fields with dark tones are bare earth.

Change-detection processing is also used to produce difference images for other remote sensing data, such as between nighttime and daytime thermal IR images (Chapter 5).

HARDWARE AND SOFTWARE FOR IMAGE PROCESSING

The image-processing routines are implemented on computer systems that consist of hardware and software, both of which are evolving at a rapid rate. For example, when the second edition of this book was written, in 1986, a typical state-of-the-art image-processing system cost several hundred thousand dollars and was supported by a supercomputer and peripheral hardware costing tens of million dollars. In 1996 a stand-alone desktop computer system costing $15,000 replaces the earlier system.

Hardware

Personal computers can be classified according to their operating system: Mac OS (Macintosh Operating System), Windows 95, or Unix. This book is not the forum to debate the relative merits of these systems. Most systems are acceptable; the choice is largely based on personal preference. Figure 8-36 shows the basic components of a typical image processing system, such as the one I use.

The data input/output components are used to read original data, such as TM, into the system. The common current formats are 8-mm tape and CD-ROM. The second function of the input/output components is to record the digitally processed data for later playback into image prints (hard copy). The output function is also used to make backup records that safeguard against loss of data.

The original TM data are loaded onto the hard drive (not shown in Figure 8-36) which stores the original data. Several different data sets (TM, SPOT, digital terrain data) may be stored and used concurrently to create a combination image. During a processing session, a number of intermediate data sets are generated and stored on the hard drive. Therefore the hard drive should have several gigabytes (10^9 bytes) of memory, which is relatively inexpensive. The data are processed by
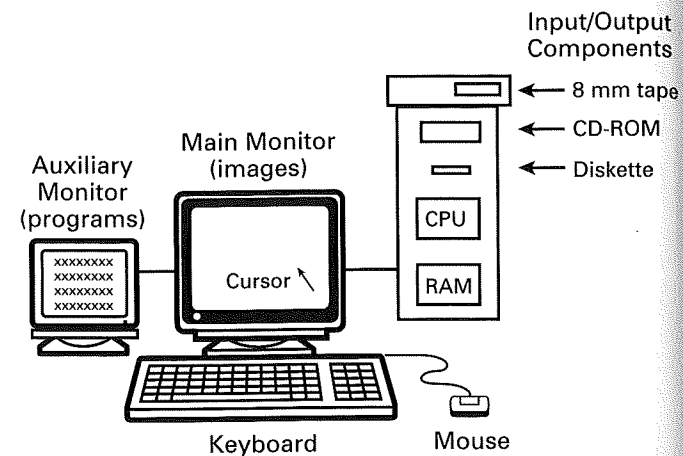

Figure 8-36 Components of a typical interactive image-processing system.

the central processing unit (CPU) which incorporates the random access memory (RAM), shown in Figure 8-36. The amount of RAM influences the speed at which the data are processed. RAM is relatively expensive, but several tens of megabytes are a minimum requirement. The system in Figure 8-36 has 96 megabytes of RAM and performs satisfactorily. New systems operate in a parallel-processing mode that accelerates processing speeds. Data are divided into subsets, typically four, which are processed simultaneously and recombined into output data.

Images and program information are shown on monitors, which are digitally controlled color display screens. Large-area, high-resolution monitors are desirable for most operations. The system in Figure 8-36 employs a second optional smaller monitor to display program information, which eliminates clutter on the large monitor. The keyboard and mouse enable the operator to interact with the system.

Software

Software is a set of instructions that commands the hardware system. A basic set of software (DOS, Apple, or Unix) is installed to operate the system. Additional application software is required for specific tasks, such as image processing. A variety of image-processing software is available for each of the three operating systems. Table 8-1 is a representative list of commercial vendors of image-processing software. All of the software packages include routines for the basic operations described in this chapter (restoration, enhancement, and information extraction), although the organization and nomenclature may be different. This book is not the forum to review the merits of different software packages, except to note that there are several ways to evaluate software:

1. Contact established users with applications similar to yours and get their opinions.
2. The Internet has bulletin boards that can be helpful.

3. Ask vendors for demonstration versions of their software that can be installed on your system for evaluation.
4. Many vendors have demonstration booths at the remote sensing conferences listed in Chapter 1, where you can try out the software.

In addition to commercial software, there are a variety of public-domain packages that are accessible via Internet. (*Note:* I am not suggesting "pirating," or copying copyrighted software. Not only is this practice illegal; it also denies compensation to the developers of the software. Without compensation, there is no incentive to develop new software that we will need in the future.)

Interactive Image-Processing Session

A typical Landsat image-processing session proceeds as follows:

1. After the CCT is loaded, the analyst selects three TM bands and assigns them to the blue, green, and red channels of the monitor. A typical combination is bands 2-4-7 shown in BGR (blue, green, and red). The TM image consists of 5667 lines, each with 6167 pixels, but the monitor in Figure 8-36 displays only 1152 lines by 870 pixels. The image is resampled to fit on the monitor; every eighth line and every eighth pixel are displayed. The mouse and on-screen cursor are used to select a representative subscene, which is displayed at full resolution with each line and pixel of original data shown on the monitor.
2. The display is examined for defects, such as banding and line dropouts, which are then restored.
3. The next step is to enhance the image. Each of the three spectral bands, together with its histogram, is viewed separately, and the contrast is enhanced. The three bands are then viewed as a color display, which typically is undersaturated. The image is transformed into its IHS components, and saturation is enhanced. At this stage it is generally useful to apply a nondirectional edge-enhancement filter to the intensity component. The image is transformed back into an enhanced BGR display. Coordinate grids (latitude and longitude; UTM) are added and the image is ready for plotting as hard copy.
4. Information extraction begins with the original data, not with the enhanced data from step 3. Images of principal components, ratios, and classifications are generated and interactively modified to suit the application.

Table 8-1 Image-processing software and vendors

Dimple Cherwell Scientific Publishing, Inc. 744 San Antonio Road, Suite 27A Palo Alto, CA 94303 Telephone: 415-852-0720 Fax: 415-852-0723	ImageStation Intergraph Corp. Huntsville, AL 35894 Telephone: 205-730-2000 Fax: 205-730-1263
EASI/PACE PCI Enterprises 50 West Wilmot Street Richmond Hill, Ontario Canada L4B 1M5 Telephone: 905-764-0614 Fax: 905-764-9604	IMAGINE ERDAS 2801 Buford Highway NE, Suite 300 Atlanta, GA 30329 Telephone: 404-248-9000 Fax: 404-248-9400
ENVI Research Systems, Inc. 2995 Wilderness Place Boulder, CO 80301 Telephone: 303-786-9900 Fax: 303-786-9909	TNTmips MicroImages, Inc. 201 North 8th Street Lincoln, NB 68508 Telephone: 402-477-9554 Fax: 402-477-9559
ER Mapper Earth Resource Mapping 4370 La Jolla Drive, Suite 900 San Diego, CA 92122 Telephone: 619-558-4709 Fax: 619-558-2657	VI²STA International Imaging Systems 1500 Buckeye Drive Milpitas, CA 95035 Telephone: 408-432-3400 Fax: 408-433-0965

COMMENTS

Digital image processing has been demonstrated in this chapter using examples of Landsat images that are available in digital form. It is emphasized, however, that any image can be converted into a digital format and processed in similar fashion. There are three major functional categories of image processing:

1. *Image restoration,* to compensate for data errors, noise, and geometric distortions introduced during the scanning, recording, and playback operations
2. *Image enhancement,* to alter the visual impact that the image has on the interpreter, in a fashion that improves the information content
3. *Information extraction,* to utilize the decision-making capability of the computer to recognize and classify pixels on the basis of their digital signatures.

In all of these operations the user should be aware of the trade-offs involved, as demonstrated in the discussion of contrast stretching.

A common query is whether the benefits of image processing are commensurate with the cost. This is a difficult question that can only be answered by the context of the user's needs. If digital filtering, for example, reveals a previously unrecognized fracture pattern that in turn leads to the discovery of major ore deposits, the cost benefits are obvious. On the other hand, it is difficult to state the cost benefits of improving the accuracy of geologic and other maps through digital processing of remote sensing data. However, it should also be noted that technical advances in software and hardware are steadily increasing the volume and complexity of the processing that can be performed, often at a reduced unit cost.

QUESTIONS

1. Many users advocate higher spatial resolution (smaller ground resolution cells) for imaging systems without considering the operational consequences. Assume that the Landsat TM ground resolution cell is reduced to 10 by 10 m. Refer to Figure 8-1, and calculate the following:
   a. Number of pixels per band
   b. Number of pixels per scene (seven bands)
   c. Ratio of new pixels divided by original (30 by 30 m) pixels
2. Chapter 1 described the AVIRIS hyperspectral aircraft scanner, which acquires images that cover 10.5 by 10.5 km with ground resolution cells that cover 20 by 20 m. Calculate the number of pixels in a single band of AVIRIS data. An AVIRIS scene consists of 224 spectral bands of data. Calculate the megabytes of data in an AVIRIS scene. Assume you have acquired complete AVIRIS coverage for the area of a TM scene. Calculate the megabytes of AVIRIS data. A CD-ROM stores 650 megabytes of data. Calculate the number of CD-ROMs required to store these AVIRIS data.
3. For Figure 8-8A replace 0 with 10 and 90 with 80. Calculate the filtered values to replace noise pixels.
4. For your particular application (forestry, geography, geology, oceanography, and so forth) of Landsat TM images, which of the contrast-enhancement methods in Figure 8-14 is optimum? Explain the reasoning for your selections and any trade-offs that might occur.
5. For Figure 8-16A replace all the 35s with 47s and all the 45s with 38s. Produce the following enhanced results:
   a. Filtered data set
   b. Profile of the revised original data
   c. Profile of your filtered data
6. For Figure 8-20B replace the 30s with 31; replace the 25s with 24. Use the appropriate filter (Figure 8-20A) to enhance the northeast-trending lineament. Record the enhanced pixels in a format similar to Figure 8-20D. Plot profile A–B for the original lineament and the enhanced lineament. Repeat the process for the northwest-trending original lineament. Calculate: a. the enhanced geometric expression; b. the enhanced brightness difference in percent.
7. For your particular application, assign priorities (most useful to least useful) for the information-extraction methods. Describe how you would apply and interpret each of the most useful procedures.

REFERENCES

Bernstein, R. and D. G. Ferneyhough, 1975, Digital image processing: Photogrammetric Engineering and Remote Sensing, v. 41, p. 1465–1476.

Bernstein, R., J. B. Lottspiech, H. J. Myers, H. G. Kolsky, and R. D. Lees, 1984, Analysis and processing of Landsat 4 sensor data using advanced image processing techniques and technologies: IEEE Transactions on Geoscience and Remote Sensing, v. GE-22, p. 192–221.

Bryant, M., 1974, Digital image processing: Optronics International, Publication 146, Chelmsford, MA.

Buchanan, M. D., 1979, Effective utilization of color in multidimensional data presentation: Proceedings of the Society of Photo-Optical Engineers, v. 199, p. 9–19.

Chavez, P. S., 1975, Atmospheric, solar, and MTF corrections for ERTS digital imagery: American Society for Photogrammetry and Remote Sensing, Proceedings of Annual Meeting, Phoenix, AZ.

Chavez, P. S., S. C. Sides, and J. A. Anderson, 1991, Comparison of three different methods to merge multiresolution and multispectral data—Landsat TM and SPOT panchromatic: Photogrammetric Engineering and Remote Sensing, v. 57, p. 295–303.

Goetz, A. F. H. and others, 1975, Application of ERTS images and image processing to regional geologic problems and geologic mapping in northern Arizona: Jet Propulsion Laboratory Technical Report 32-1597, Pasadena, CA.

Haralick, R. M., 1984, Digital step edges from zero crossing of second directional filters: IEEE Transactions on Pattern Analysis and Machine Intelligence, v. PAMI-6, p. 58–68.

Jensen, J. R., 1986, Introductory digital image processing—a remote sensing perspective: Prentice-Hall, Englewood Cliffs, NJ.

Leick, A., 1995, GPS satellite surveying, second edition: John Wiley & Sons, New York, NY.

Loéve, M., 1955, Probability theory: D. van Nostrand Co., Princeton, NJ.

Moik, H., 1980, Digital processing of remotely sensed images: NASA SP 431, Washington, DC.

NASA, 1983, Thematic mapper computer compatible tape: NASA Goddard Space Flight Center Document LSD-ICD-105, Greenbelt, MD.

Rifman, S. S., 1973, Digital rectification of ERTS multispectral imagery: Symposium on Significant Results Obtained from ERTS-1, NASA SP-327, p. 1131–1142.

Rifman, S. S. and others, 1975, Experimental study of application of digital image processing techniques to Landsat data: TRW Systems Group Report 26232-6004-TU-00 for NASA Goddard Space Flight Center Contract NAS 5-20085, Greenbelt, MD.

Schowengerdt, R. A., 1983, Techniques for image processing and classification in remote sensing: Academic Press, New York, NY.

Snyder, J. P., 1987, Map projections—a working manual: U.S. Geological Survey Professional Paper 1395.

Swain, P. H. and S. M. Davis, 1978, Remote sensing—the quantitative approach: McGraw-Hill Book Co., New York, NY.

ADDITIONAL READING

Arlinghaus, S. L., ed., 1994, Practical handbook of digital mapping: CRC Press, Boca Raton, FL.

Campbell, N. A., 1966, The decorrelation stretch transformation: International Journal of Remote Sensing, v. 17, p. 1939–1949.

Harris, J. R. and others, 1994, Computer-enhancement techniques for the integration of remotely sensed, geophysical, and thematic data for the geosciences: Canadian Journal of Remote Sensing, v. 20, p. 210–221.

Mayers, M. and L. Wood, 1988, Selected annotated bibliographies for adaptive filtering of digital image data: U.S. Geological Survey Open File Report 88-104.

Popp, T., 1995, Correcting atmospheric masking to retrieve the spectral albedo of land surfaces from satellite measurements: International Journal of Remote Sensing, v. 16, p. 3483–3508.

Russ, J. C., 1995, The image processing handbook: CRC Press, Boca Raton, FL.

Verbyla, D., 1995, Satellite remote sensing of natural resources: Lewis Publishers, Boca Raton, FL.